International Journal of Heat and Mass Transfer 273 (2027) 129677

Contents lists available at ScienceDirect

International Journal of Heat and Mass Transfer

journal homepage: www.elsevier.com/locate/hmt

Hot shapes: Nusselt numbers for superellipsoidal particles suspended in Stokes flow

Jana Wedel [a,b,*], Ivan Dominik Horvat [b], Matjaž Hriberšek [b], Paul Steinmann [a,c], Jure Ravnik [b]

[a] Institute of Applied Mechanics, Friedrich-Alexander-Universität Erlangen-Nürnberg, Germany
[b] Faculty of Mechanical Engineering, University of Maribor, Slovenia
[c] Glasgow Computational Engineering Center, University of Glasgow, United Kingdom

ARTICLE INFO

Keywords:
Nusselt number
Micron-sized particles
Superellipsoids
Nusselt number neural network model
Nusselt number correlation model
Euler–Lagrange particle flow simulations

ABSTRACT

Convective heat transfer between micron-sized particles and a surrounding viscous fluid plays a crucial role in a wide range of applications, including aerosol transport, particulate flows, and particle inhalation modeling. Although spherical and ellipsoidal particles have been studied extensively regarding their convective heat transfer characteristics, accurate convective heat transfer models for irregularly shaped particles remain scarce. In this work, we consider convective heat transfer from non-spherical particles of superellipsoidal shape in the (local) Stokes-flow regime characterized by a small particle Reynolds number to learn surrogate models for the corresponding Nusselt number, characterizing the convective heat transfer between a particle and a fluid. We provide a unified framework that captures the influence of particle shape and flow conditions at small Péclet numbers. Direct numerical simulations are performed for superellipsoidal particles in creeping flow, consistent with the assumptions underlying Lagrangian point-particle approaches for particles suspended in typical fluids such as air and water. Like this, we evaluate the Nusselt number from surface-resolved and surface-integrated heat fluxes and analyze it as a function of the particle shape, its orientation, and flow conditions. We demonstrate that at small Péclet numbers ($\mathrm{Pe} \lesssim 1$) the particle orientation has a negligible influence on convective heat transfer. Focusing on small Péclet numbers we learn a Nusselt number correlation model and a physics-constrained neural-network model that predict the Nusselt number at small Péclet numbers as a function of particle shape and flow conditions. The resulting surrogate models achieve excellent predictive accuracy and enable efficient evaluation of particle–fluid convective heat transfer in the Lagrangian point-particle setting for a broad class of non-spherical particles.

1. Introduction

Particle-laden flows are ubiquitous in natural and engineering systems, including aerosol transport, environmental exposure, and energy applications. For dilute particle-laden flows in which the particle characteristic size is sufficiently small compared with the relevant length scales of the undisturbed carrier-flow field, a Lagrangian point-particle approach provides a computationally efficient modeling framework. In this approach, individual particles are tracked without resolving their surfaces or the associated particle-scale disturbance fields.

When thermal effects are concerned, the heat convection between a particle and the surrounding fluid is overall encapsulated in the Nusselt number (see Eq. (16)), that is, the dimensionless heat-transfer coefficient, which is generally dependent on the shape of the particle, its orientation, the flow conditions, and the thermophysical properties of the fluid.[1] It essentially represents the particle surface-averaged ratio between the convective and conductive heat transfer at the particle–fluid interface, and it is generally not known a priori, but must be modeled.

Empirical models for the Nusselt number exist, however, most commonly for spherical particles. In the Stokes-flow limit and as a baseline, the Nusselt number for spherical particles is constant with $\mathrm{Nu}(\mathrm{Re}_\mathrm{p} \to 0) = 2$. Here, Re_p denotes the particle Reynolds number (see Eq. (1)) based on the particle–fluid slip velocity, the particle diameter, and the fluid kinematic viscosity. It measures the relative importance of fluid-inertia and viscous effects in the particle-scale flow. For the non-spherical particles considered below, the characteristic diameter is taken as the volume-equivalent diameter d_eq.

For finite particle Reynolds numbers, one of the most widely used empirical models for the Nusselt number is by Ranz and Marshall [1].

* Corresponding author at: Institute of Applied Mechanics, Friedrich-Alexander-Universität Erlangen-Nürnberg, Germany.
E-mail address: jana.wedel@fau.de (J. Wedel).

[1] In the present study, T_f^∞ and the particle surface temperature, thus ΔT, are prescribed and the particle is treated as isothermal. Consequently, particle thermal properties, such as the thermal conductivity and heat capacity, do not enter the particle-scale heat-transfer problem explicitly.

https://doi.org/10.1016/j.ijheatmasstransfer.2026.129677
Received 29 June 2026; Received in revised form 9 September 2026; Accepted 28 September 2026
Available online 14 October 2026
0017-9310/© 2026 Published by Elsevier Ltd.

Later, the popular model for the Nusselt number by Whitaker [2] was proposed. When comparing both models the results can deviate by up to 10%, [3]. Various further refinements have been proposed to improve both the accuracy and the validity range of these Nusselt number models; see, for example, [4,5].

Compared with the extensive literature available for spherical particles, a smaller but substantial body of work has addressed heat and mass transfer from non-spherical particles using analytical, numerical, and empirical approaches. Nevertheless, most models for the Nusselt number proposed for non-spherical particles are generally valid only in restricted scenarios [3].

Foundational theoretical results were obtained by Brenner [6], who studied forced-convection heat and mass transfer at small Péclet numbers from a particle of arbitrary shape. His analysis established a general asymptotic description of the leading convective correction in the low-Pe limit. Acrivos [7] subsequently investigated heat or mass transfer from a small particle of arbitrary shape freely suspended in a linear shear flow. These studies demonstrate that general analytical results can be derived for arbitrary particle shapes in asymptotic transport regimes.

Several numerical studies have considered specific classes of non-spherical particles and proposed corresponding Nusselt-number correlations. Dwyer and Dandy [8] investigated the effects of ellipsoidal particle shape and orientation on drag and heat transfer at intermediate Reynolds numbers, $10 \leq \mathrm{Re_p} \leq 66$. The correlation of Churchill and Bernstein [9] describes the Nusselt number of a circular cylindrical fiber in crossflow and covers a broad range of flow regimes ($\mathrm{Re_p}\,\mathrm{Pr} < 0.2$, where Pr denotes the Prandtl number). Its accuracy is, however, limited, with deviations of approximately 20% reported in Ref. [10]. Other engineering models frequently describe non-sphericity through averaged quantities or empirical shape factors [11], while several shape-dependent correlations have been developed for specific applications [12]. Richter and Nikrityuk [13] investigated heat transfer from ellipsoidal and cubic particles at varying inclination angles ϕ, a prescribed temperature ratio, and a fixed aspect ratio, i.e. half-axis ratio, $\lambda = 2$. Based on their numerical results, they proposed correlations for particle dynamics and the Nusselt number for $\mathrm{Re_p} \leq 200$, $0° \leq \phi \leq 90°$. Kishore and Gu [14] investigated momentum and heat transfer from spheroidal particles, further demonstrating the influence of particle geometry and orientation on the transport characteristics. Similarly, Ke et al. [15] examined a fixed, heated ellipsoidal particle and analyzed the effects of particle aspect ratio, inclination angle, and Reynolds number. Based on 125 numerical simulations, they derived a correlation valid for $0.25 \leq \lambda \leq 2.5$, $0° \leq \phi \leq 90°$, $10 \leq \mathrm{Re_p} \leq 200$. Ma and Zhao [16] performed Immersed Boundary Method (IBM) coupled with the Lattice Boltzmann Method (LBM) simulations of forced-convection heat transfer from a heated, stationary rod-like particle in a uniform flow. They considered $1 \leq \mathrm{Re_p} \leq 1500$, $1 \leq \lambda_1 \leq 5$, $0° \leq \phi \leq 90°$. Their results showed that particle aspect ratio and orientation have only a minor influence on the Nusselt number at low Reynolds numbers, whereas their effects become more pronounced and exhibit different trends at intermediate and high Reynolds numbers. Based on their numerical database, they proposed a Nusselt-number correlation that accounts for the effects of $\mathrm{Re_p}$, particle aspect ratio λ_1, and particle orientation ϕ. Kiwitt et al. [3] performed particle-resolved simulations of a fixed prolate ellipsoid maintained at constant temperature in a uniform flow. Their parameter range covered $1 \leq \mathrm{Re_p} \leq 100$, $0° \leq \phi \leq 90°$, $0.25 \leq \lambda \leq 2.5$, and they developed a corresponding Nusselt-number correlation. More recently, Lote et al. [17] performed particle-resolved simulations of heat and fluid flow around prolate ellipsoidal and cylindrical particles for $2 \leq \lambda_1 \leq 10$, $0° \leq \phi \leq 90°$, $0.1 \leq \mathrm{Re_p} \leq 300$. Based on their numerical results, they proposed correlations for the Nusselt number, drag coefficient, lift coefficient, and pitching-torque coefficient, explicitly accounting for particle shape and orientation. Their results showed that the Nusselt number generally increases with both $\mathrm{Re_p}$ and the incidence angle, whereas the differences between prolate and cylindrical particles decrease with increasing aspect ratio. Xu et al. [18] investigated heat transfer and fluid flow around oblate particles over the ranges $0.2 \leq \lambda_1 \leq 1$, $0° \leq \phi \leq 90°$, $0.1 \leq \mathrm{Re_p} \leq 2000$. Based on particle-resolved simulations, they proposed correlations for the Nusselt number and aerodynamic coefficients, with reported mean relative errors below 7% over the investigated parameter range.

The available theoretical studies thus establish general asymptotic results for arbitrary shapes, whereas the numerical correlations provide quantitative predictions for selected particle shapes (most commonly spheroidal, ellipsoidal, cylindrical, rod-like particles) and parameter ranges. They typically vary one aspect ratio and one inclination angle.

Although the reported studies are a valuable tool for engineering analyses, the lack of accurate models for the Nusselt number of more arbitrary non-spherical particles poses a significant limitation for Lagrangian point-particle simulations of particle-laden flows.

Superellipsoids [19] are particularly useful in this context because they provide a compact and continuous representation of a broad range of three-dimensional particle geometries within a single parametrization. The aspect ratios λ_1 and λ_2 control particle elongation and flattening, whereas the shape exponents s_1 and s_2 control the distribution of surface curvature and enable continuous transitions between rounded, block-like, and pointed geometries. Allowing $s_1 \neq s_2$ further permits the representation of particles with asymmetric curvature distributions.

This continuous shape description is especially well suited to surrogate modeling, because it allows the Nusselt number to be learned as a continuous function of a small set of geometric parameters, rather than requiring separate correlations for spheres, ellipsoids, cubes, rods, and plates. It is also compatible with Lagrangian point-particle formulations, for which storing a compact set of shape parameters is considerably more practical than retaining a fully resolved particle surface.

Note that the asymptotic theories of Brenner and Acrivos [6,7] provide general low-Pe results for particles of arbitrary shape, but they do not directly yield a ready-to-use quantitative model over the multidimensional superellipsoidal shape space considered here. In particular, evaluation of the leading-order contribution requires the shape-dependent pure-conduction solution, while higher-order terms in Brenner's formulation additionally depend on the hydrodynamic resistance, and hence on the drag force for the prescribed particle motion. These shape-dependent quantities must therefore be known separately for the particle geometry considered. Moreover, the accuracy of a strict small-Pe expansion is not guaranteed over a finite interval extending to $\mathrm{Pe} = O(1)$, and the combined dependence on independently varying aspect ratios, shape exponents, and imposed flow direction is not available in a form suitable for direct implementation in a point-particle model. Consequently, a unified quantitative description that continuously accounts for anisotropy, blockiness, multiple aspect ratios, and relative-flow direction across the complete superellipsoidal parameter space is still lacking.

The present work addresses this gap by generating a particle-resolved DNS database and developing directly evaluable surrogate models for the Nusselt number over the prescribed finite parameter domain. The contribution is therefore not a new general low-Pe asymptotic theory, but rather a shape-resolved and practically applicable extension that complements the theoretical results of Brenner and Acrivos by quantifying the dependence of heat transfer on the complete superellipsoidal geometry and the imposed relative-flow direction.

To address this gap, we perform particle-resolved direct numerical simulations that explicitly resolve the velocity and temperature fields in the vicinity of the particle–fluid interface for a broad range of superellipsoidal particle shapes, imposed relative-flow directions, and Péclet numbers. From the resulting surface-resolved heat fluxes, we determine the particle-surface-averaged heat-transfer coefficient and the corresponding Nusselt number.

Analysis of the DNS database reveals three distinct transport regimes. For $\mathrm{Pe} \leq 0.01$, the Nusselt number is effectively governed by particle

shape alone. In the intermediate range $0.01 < \mathrm{Pe} \lesssim 1$, both particle shape and the Péclet number influence the heat transfer, whereas for $\mathrm{Pe} > 1$ the particle orientation relative to the imposed flow becomes an additional relevant variable. Based on these observations, the surrogate models developed in the present work are restricted to $\mathrm{Pe} \lesssim 1$, for which the orientation dependence remains negligible over the investigated shape space.

In the particle-resolved simulations, the particle surface temperature is prescribed. In the intended Lagrangian point-particle application, the resulting Nusselt-number models provide the heat-transfer closure required to evolve the particle temperature under the lumped-capacitance assumption. For sufficiently small particle Biot numbers (see Appendix A, Eq. (A.3)), internal temperature gradients may be neglected and the particle can be treated as thermally uniform, while its temperature remains generally time dependent. This assumption does not imply instantaneous thermal equilibrium with the surrounding fluid. Instead, the particle temperature evolves over a finite thermal response time according to the particle energy balance, which requires an accurate case-dependent interphase heat-transfer coefficient.

The present study is restricted to the creeping-flow regime, $\mathrm{Re}_\mathrm{p} \ll 1$, consistently with the point-particle framework adopted in our previous works [20,21]. Corrections associated with low but finite particle Reynolds numbers are not included in the present formulation and may modify both the hydrodynamic and thermal transport around the particle.

Within this scope, the objective of the present work is to develop unified surrogate models for the Nusselt number that account continuously for non-spherical particle geometry and flow conditions. To this end, we generate a particle-resolved DNS database over a multidimensional superellipsoidal shape space and construct directly evaluable Nusselt-number models for implementation in Lagrangian point-particle simulations. To the best of our knowledge, no previous study has provided such a unified description for superellipsoidal particles that independently accounts for multiple aspect ratios, shape exponents, and the imposed relative-flow direction. The proposed models therefore enable efficient and shape-resolved prediction of particle–fluid convective heat transfer for a broad class of non-spherical particles within the investigated Stokes-flow and Péclet-number ranges.

2. Problem setting

The heat transfer problem considered here consists of a micron-sized rigid solid particle immersed in a surrounding fluid, as shown in the particle-resolved schematic in Fig. 1.

2.1. Preliminaries

The particle considered is of generic shape with volume-equivalent diameter d_eq, which defines the characteristic size of the problem. The interface between the particle and the fluid, that is, the particle boundary, is denoted by Γ. The unit normal vector that points from the particle into the fluid is $\boldsymbol{n} := \boldsymbol{n}^\mathrm{s} = -\boldsymbol{n}^\mathrm{f}$ with $\boldsymbol{n}^\mathrm{f}$ the reverse direction, that is, the unit normal that points from the fluid into the particle.

The flow is characterized by the relative velocity $\boldsymbol{u} := \boldsymbol{v}_\mathrm{f}^\infty - \boldsymbol{v}_\mathrm{s}$ between the ambient flow velocity $\boldsymbol{v}_\mathrm{f}^\infty$ and the particle velocity $\boldsymbol{v}_\mathrm{s}$ and has magnitude $U := |\boldsymbol{u}|$, which defines the characteristic flow velocity of the problem. The fluid is thermally characterized by its local temperature field $T_\mathrm{f} = T_\mathrm{f}(\boldsymbol{x}, t)$ and by the undisturbed ambient-fluid temperature T_f^∞ prescribed away from the particle. Its material parameters, assumed constant, are: density ρ^f, specific heat capacity (at constant pressure) c_p^f, thermal conductivity k^f, and dynamic and kinematic viscosity μ^f and $\nu^\mathrm{f} := \mu^\mathrm{f}/\rho^\mathrm{f}$, respectively. The particle is thermally characterized by its (possibly uniform) temperature field $T_\mathrm{s} = T_\mathrm{s}(\boldsymbol{x}, t)$ with trace T_s^Γ at the particle–fluid interface denoted the surface temperature. Its material parameters, assumed constant, are: density ρ^s, specific heat capacity (at constant pressure) c_p^s, and thermal conductivity k^s. The characteristic temperature of the problem is defined as the temperature difference $\Delta T := T_\mathrm{s}^\Gamma - T_\mathrm{f}^\infty$ between the surface temperature of the particle and the ambient temperature of the fluid.

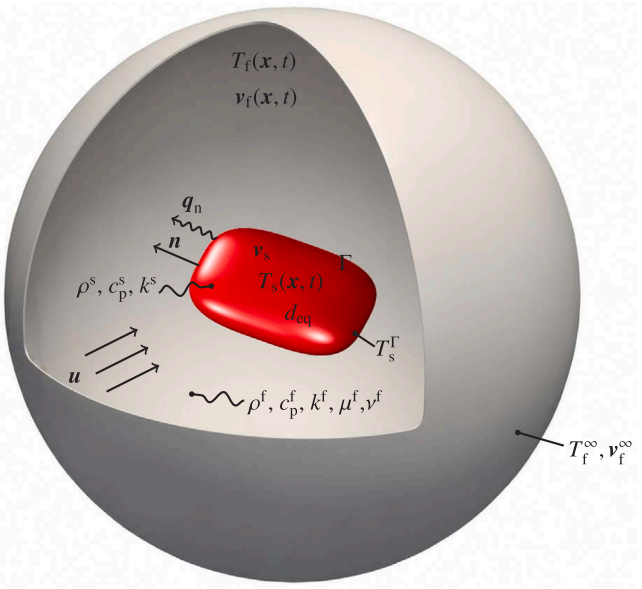


Fig. 1. Particle-resolved view: A particle of volume-equivalent diameter d_eq (here depicted as superellipsoid with $\lambda_1 = 3$, $\lambda_2 = 2$, $s_1 = 1.0, s_2 = 0.6$) immersed in fluid flow. Note that the particle was enlarged for visualization for the sake of presentation.

2.2. Governing equations for the fluid

The flow regime around the particle is characterized by the dimensionless particle Reynolds number

$$\mathrm{Re}_\mathrm{p} := \frac{U\, d_\mathrm{eq}}{\nu^\mathrm{f}}. \tag{1}$$

Observe that Re_p depends on the particle size d_eq, the particle–fluid slip velocity U, and the fluid kinematic viscosity ν^f. Recall that the present study is restricted to the creeping-flow regime, $\mathrm{Re}_\mathrm{p} \ll 1$, in which viscous effects dominate over fluid inertia. The steady particle-scale flow is therefore governed by the incompressible Stokes equations

$$\boldsymbol{\nabla} \cdot \boldsymbol{v}_\mathrm{f} = 0 \qquad \text{in } \Omega_\mathrm{f}, \tag{2}$$

$$-\boldsymbol{\nabla} p_\mathrm{f} + \mu^\mathrm{f} \nabla^2 \boldsymbol{v}_\mathrm{f} = \boldsymbol{0} \qquad \text{in } \Omega_\mathrm{f}, \tag{3}$$

where Ω_f denotes the fluid domain and p_f is the pressure field that enforces incompressibility. In the particle-fixed reference frame, the no-slip condition at the particle surface Γ is

$$\boldsymbol{v}_\mathrm{f} = \boldsymbol{0} \qquad \text{on } \Gamma. \tag{4}$$

The imposed particle–fluid relative velocity is prescribed at the outer boundary Γ_∞ as

$$\boldsymbol{v}_\mathrm{f} = \boldsymbol{u} \qquad \text{on } \Gamma_\infty. \tag{5}$$

For each prescribed particle geometry and relative velocity $\boldsymbol{u}$, this steady Stokes boundary-value problem is solved using OpenFOAM [22].

Furthermore, the fluid temperature field $T_\mathrm{f} = T_\mathrm{f}(\boldsymbol{x}, t)$ is in general governed by an instationary temperature evolution equation of advection–diffusion type

$$\rho^\mathrm{f} c_\mathrm{p}^\mathrm{f} \left[\frac{\partial T_\mathrm{f}}{\partial t} + \boldsymbol{v}_\mathrm{f} \cdot \boldsymbol{\nabla} T_\mathrm{f} \right] = -\boldsymbol{\nabla} \cdot \boldsymbol{q}^\mathrm{f} \qquad \text{in } \Omega_\mathrm{f}, \quad \boldsymbol{q}^\mathrm{f} = -k^\mathrm{f} \boldsymbol{\nabla} T_\mathrm{f}, \tag{6}$$

where the fluid heat flux is described by Fourier's law. In the present study, the particle geometry, the particle–fluid slip velocity, and the thermal boundary conditions are prescribed and time independent. The surrounding velocity field is obtained from the steady Stokes equations. We subsequently consider the corresponding steady thermal response, that is, the temperature field after transient thermal effects have decayed. Accordingly, the transient term in the fluid energy equation is omitted.

Under these assumptions, the fluid temperature field $T_\mathrm{f} = T_\mathrm{f}(\boldsymbol{x})$ is governed by the stationary advection–diffusion equation

$$\boldsymbol{v}_\mathrm{f} \cdot \boldsymbol{\nabla} T_\mathrm{f} = \alpha^\mathrm{f} \nabla^2 T_\mathrm{f} \qquad \text{in } \Omega_\mathrm{f}, \qquad \alpha^\mathrm{f} := \frac{k^\mathrm{f}}{\rho^\mathrm{f} c_\mathrm{p}^\mathrm{f}}, \tag{7}$$

where α^f denotes the fluid thermal diffusivity. The particle is maintained at a prescribed uniform surface temperature,

$$T_\mathrm{f} = T_\mathrm{s}^\Gamma \qquad \text{on } \Gamma, \tag{8}$$

while the undisturbed ambient-fluid temperature is imposed at the outer boundary,

$$T_\mathrm{f} = T_\mathrm{f}^\infty \qquad \text{on } \Gamma_\infty. \tag{9}$$

For each previously computed particle-scale velocity field $\boldsymbol{v}_\mathrm{f}$, the stationary thermal boundary-value problem is solved using OpenFOAM.

Note that in the numerical simulations, the temperature difference is normalized to $\Delta T = 1$. Because the fluid thermophysical properties are assumed constant and buoyancy is neglected, the stationary temperature equation is linear in ΔT. Accordingly, the computed heat flux scales linearly with ΔT, whereas the resulting heat-transfer coefficient and Nusselt number are independent of its magnitude. The results can therefore be rescaled to an arbitrary dimensional temperature difference, provided that temperature-dependent material properties and buoyancy effects remain negligible.

In the sequel, two further dimensionless parameters characterizing the thermo-mechanical flow conditions are of relevance, that is, the Prandtl (Pr) number and the Péclet (Pe) number, respectively,

$$\mathrm{Pr} := \frac{\nu^\mathrm{f}}{\alpha^\mathrm{f}} \quad \text{and} \quad \mathrm{Pe} := \frac{U\, d_\mathrm{eq}}{\alpha^\mathrm{f}}. \tag{10}$$

The particle Péclet number measures the relative importance of advective and diffusive thermal transport around the particle. Equivalently,

$$\mathrm{Pe} = \frac{d_\mathrm{eq}^2/\alpha^\mathrm{f}}{d_\mathrm{eq}/U} = \frac{\tau_\mathrm{diff}}{\tau_\mathrm{adv}}, \tag{11}$$

where $\tau_\mathrm{diff} = d_\mathrm{eq}^2/\alpha^\mathrm{f}$ is the characteristic thermal diffusion time and $\tau_\mathrm{adv} = d_\mathrm{eq}/U$ is the characteristic advection time. Accordingly, $\mathrm{Pe} \ll 1$ denotes diffusion-dominated heat transfer, $\mathrm{Pe} = \mathcal{O}(1)$ indicates comparable advective and diffusive transport, and $\mathrm{Pe} \gg 1$ denotes advection-dominated transport.

Observe that the Péclet number relates to the Prandtl number via the particle Reynolds number through

$$\mathrm{Pe} = \mathrm{Re_p}\,\mathrm{Pr}\,. \tag{12}$$

Experimental investigations of small inertial particles in turbulent wall-bounded flows have demonstrated measurable differences between the particle and carrier-fluid velocities. Kiger et al. [23] reported nonzero particle–fluid relative motion in a particle-laden turbulent channel flow, with the slip depending on the velocity component and the position within the channel. Fong et al. [24] experimentally observed that size-selected glass microspheres in turbulent channel flow did not follow the carrier-flow velocity uniformly, particularly in the near-wall region, where enhanced particle velocity fluctuations and random uncorrelated motion were reported. Esmaily et al. [25] investigated small, heavy inertial particles in turbulent duct flow using experimental and computational methods. Particle-resolved simulations have likewise revealed large apparent particle–fluid slip velocities for small inertial particles close to the wall [26].

The following air- and water-based values are illustrative conversions. For example, in air with $\mathrm{Pr} \approx 0.7$, particle Reynolds numbers $\mathrm{Re_p} = 0.1$, 0.5, and 1 correspond to $\mathrm{Pe} \approx 0.07$, 0.35, and 0.7, respectively. In water with $\mathrm{Pr} \approx 7$, the same Reynolds numbers correspond to $\mathrm{Pe} \approx 0.7$, 3.5, and 7. These representative conversions show that $\mathrm{Pe} \leq 1$ cannot be inferred from particle size or from the creeping-flow condition alone. Since $\mathrm{Pe} = \mathrm{Re_p}\,\mathrm{Pr}$, fluids with large Prandtl numbers may exhibit $\mathrm{Pe} > 1$ even when $\mathrm{Re_p} \ll 1$. The range $\mathrm{Pe} \leq 1$ considered here therefore denotes the investigated and validated range of the proposed surrogate models rather than a universal upper limit for particles in the Stokes-flow regime. The present models are consequently most directly applicable to conditions for which the resulting particle Péclet number remains within this range. For completeness, the general particle-energy balance and the lumped-capacitance formulation relevant to the intended point-particle application are provided in Appendix A.

2.3. Interface conditions between the fluid and the particle

In the particle-resolved description, the heat flux is normal continuous at the fluid–particle interface Γ, that is, its jump across Γ vanishes in normal direction; thus, the scalar-valued (normal) heat flux from the particle into the fluid is likewise expressed as

$$q_\mathrm{n} = \boldsymbol{q}^\mathrm{s} \cdot \boldsymbol{n} \equiv \boldsymbol{q}^\mathrm{f} \cdot \boldsymbol{n}\,, \tag{13}$$

where $\boldsymbol{n}$ denotes the unit normal directed from the particle into the fluid.

Note that in the present simulations, the uniform particle-surface temperature T_s^Γ is prescribed, and the resulting normal heat flux q_n is evaluated from the computed fluid-temperature field. The effective convective heat-transfer coefficient is then defined through the surface-averaged relation

$$h\,\langle \Delta T \rangle_\Gamma = \langle q_\mathrm{n} \rangle_\Gamma \quad \text{with} \quad \Delta T := T_\mathrm{s}^\Gamma - T_\mathrm{f}^\infty\,, \tag{14}$$

where

$$\langle q_\mathrm{n} \rangle_\Gamma := \frac{1}{A} \int_\Gamma q_\mathrm{n}\, \mathrm{d}A. \tag{15}$$

This relation is used to determine the effective heat-transfer coefficient a posteriori and is not imposed as a Robin boundary condition in the particle-resolved simulations. Observe that the convective heat transfer coefficient $h \geq 0$ is here assumed constant along Γ. It depends in general on the particle shape, its orientation and the flow conditions. Thus, it is not known a priori and needs to be determined in a case-dependent fashion. It is typically expressed in terms of the dimensionless Nusselt number Nu, which expands as

$$\mathrm{Nu} := \frac{h\, d_\mathrm{eq}}{k^\mathrm{f}}\,. \tag{16}$$

The Nusselt number Nu captures the ratio of convective heat transfer through the particle–fluid interface to the conductive heat transfer in the fluid. As a particle-surface-averaged quantity, it encapsulates the combined influence of particle shape, orientation, and flow conditions on convective heat transfer and thus constitutes the central quantity of interest in this work.

2.4. Decoupling of flow and temperature in the fluid

In general, flow and temperature in fluids are thermally coupled through buoyancy, as temperature differences in the fluid may induce density variations and thereby modify the momentum balance. The importance of this coupling can be assessed by the Richardson number (Ri). In the present context the Richardson number relates the working of the buoyancy force $g\,\rho^\mathrm{f}\,d_\mathrm{eq}^3$ of a fluid element along the thermal expansion $\beta^\mathrm{f}\,\Delta T\,d_\mathrm{eq}$ of the fluid to the kinetic energy of the

flow $\rho^{\mathrm{f}}\, d_{\mathrm{eq}}^3\, U^2$, where g is the gravitational acceleration and β^{f} is the volumetric thermal expansion coefficient of the fluid, and thus results in

$$\mathrm{Ri} := \frac{g\,\beta^{\mathrm{f}}\,\Delta T\,d_{\mathrm{eq}}}{U^2} = \frac{\mathrm{Gr}}{\mathrm{Re}_{\mathrm{p}}^2}, \qquad \text{where} \qquad \mathrm{Gr} := \frac{g\,\beta^{\mathrm{f}}\,\Delta T\,d_{\mathrm{eq}}^3}{\left[\nu^{\mathrm{f}}\right]^2} \tag{17}$$

is the Grashof number. In this work we focus on the regime $\mathrm{Ri} \ll 1$, where the coupling of flow and temperature in the fluid is negligible. Note that assumptions $\mathrm{Re}_{\mathrm{p}} \ll 1$ and $\mathrm{Ri} \ll 1$ represent two independent restrictions. The first permits the neglect of fluid-inertia effects, whereas the second permits the neglect of buoyancy. In particular, $\mathrm{Re}_{\mathrm{p}} \ll 1$ does not by itself imply $\mathrm{Ri} \ll 1$, because at fixed Gr the Richardson number increases as Re_{p} decreases. Negligible buoyancy additionally requires $U \gg \sqrt{g\,\beta^{\mathrm{f}}\,\Delta T\,d_{\mathrm{eq}}}$. The present study is restricted to physical conditions satisfying both $\mathrm{Re}_{\mathrm{p}} \ll 1$ and $\mathrm{Ri} \ll 1$. It therefore represents forced convection in the creeping-flow regime. Under this assumption, the temperature field acts as a passive scalar and does not modify the momentum equation. Consequently, we first solve the steady Stokes problem for the velocity field and subsequently use the resulting $\boldsymbol{v}_{\mathrm{f}}$ in the stationary advection–diffusion equation.

2.5. DNS computation of the Nusselt number

Finally, for the lumped-capacitance assumption (described in Appendix A) with $\Delta T \equiv \langle \Delta T \rangle_{\Gamma}$ the convective heat transfer coefficient h follows from the averaged convective interface condition in Eq. (14) to result in $h = \langle q_{\mathrm{n}} \rangle_{\Gamma} / \Delta T$.

Thus, in the current scenario we will determine the Nusselt number $\mathrm{Nu} = h\,d_{\mathrm{eq}}/k^{\mathrm{f}}$ by evaluating, through detailed DNS computations of the scalar-valued (normal) heat flux $q_{\mathrm{n}} = \boldsymbol{q}^{\mathrm{f}} \cdot \boldsymbol{n}$ around the fully resolved particle surface, the expression

$$\mathrm{Nu} = \frac{d_{\mathrm{eq}}}{k^{\mathrm{f}}\,\Delta T\,A} \int_{\Gamma} q_{\mathrm{n}}\,\mathrm{d}A\,. \tag{18}$$

The interface integral on the right-hand side denotes the resultant scalar-valued (normal) heat flux (aka the thermal power) transferred through the particle–fluid interface by convection. In summary, the Nusselt number as given in Eq. (18) provides a computable dimensionless measure of the convective interfacial heat transfer; it constitutes the central quantity of interest in this contribution. Operationally, in the particle-resolved view, we perform the necessary DNS computations by solving the Stokes equations for the fluid velocity $\boldsymbol{v}_{\mathrm{f}}$ and the advection–diffusion equation for the fluid temperature T_{f} in a staggered fashion, using a custom finite-volume solver implemented within OpenFOAM v11 [22].

A mesh-convergence study was performed to verify that the numerical resolution in the vicinity of the particle is sufficient for converged predictions of the surface-integrated heat flux and Nusselt number. Details of the computational domain, boundary conditions, mesh refinement, convergence assessment and additional validation against analytical heat-transfer and drag-force solutions are provided in Appendix B.

2.6. Numerical procedure and validation

The particle-resolved simulations are performed using a custom solver implemented in OpenFOAM v11 [22].[2]

The governing equations are discretized using the cell-centered finite-volume method implemented in OpenFOAM v11 [22]. The Stokes equations are solved using the SIMPLE algorithm, with Gauss-linear spatial discretization and non-orthogonality correction. The stationary temperature equation is solved sequentially using a bounded limitedLinear scheme for advection and a Gauss-linear corrected scheme for diffusion. Pressure, velocity, and temperature are solved using GAMG, smoothSolver, and PBiCGStab, respectively. For each prescribed particle geometry and relative-flow direction, the steady incompressible Stokes equations are solved first. The resulting velocity field $\boldsymbol{v}_{\mathrm{f}}$ is subsequently used in the stationary advection–diffusion equation for the fluid temperature. The flow and thermal problems are therefore solved sequentially in a staggered manner.

The particle is fixed at the center of a spherical computational domain with diameter $D = 1024\,d_{\mathrm{eq}}$. This domain size follows the domain-size analysis of Strakl et al. [27], who showed that $D = 1024\,d_{\mathrm{eq}}$ provides an adequate approximation of the unbounded Stokes-flow condition for superellipsoidal particles. The same computational domain is used for the thermal problem, whose numerical accuracy is assessed in Appendix B. In the particle-fixed reference frame, the velocity boundary conditions are

$$\boldsymbol{v}_{\mathrm{f}} = \boldsymbol{0} \qquad \text{on } \Gamma, \tag{19}$$

$$\boldsymbol{v}_{\mathrm{f}} = \boldsymbol{u} \qquad \text{on } \Gamma_{\infty}. \tag{20}$$

The particle surface is maintained at a prescribed uniform temperature, while the ambient-fluid temperature is imposed at the outer boundary,

$$T_{\mathrm{f}} = T_{\mathrm{s}}^{\Gamma} \qquad \text{on } \Gamma, \tag{21}$$

$$T_{\mathrm{f}} = T_{\mathrm{f}}^{\infty} \qquad \text{on } \Gamma_{\infty}. \tag{22}$$

The computational mesh is refined in the vicinity of the particle surface in order to resolve the local velocity and temperature gradients and the resulting normal heat flux. Four successively refined meshes, denoted by M0–M3, were considered. The mesh M2, containing approximately 5.1×10^4 cells for the spherical reference case and 2336 particle-surface elements, was selected for the subsequent simulations as a compromise between numerical accuracy and computational cost.

The numerical implementation was validated using analytical reference solutions for a spherical particle. Under Stokes-flow conditions, the computed drag force was compared with

$$F_{\mathrm{sph,Stk}} = 3\pi\mu^{\mathrm{f}}\,d_{\mathrm{eq}}U.$$

For mesh M2, the relative deviation from the analytical Stokes drag was −0.282%. The thermal solver was assessed at $\mathrm{Pe} = 0.001$ using the pure-conduction limit $\mathrm{Nu} = 2$ for a sphere. The corresponding numerical result was $\mathrm{Nu} = 1.9884$, representing a relative deviation of −0.580%.

Additional mesh-convergence studies were performed for representative prolate, oblate, cubical, and diamond-shaped particles. For the selected mesh M2, the changes in the computed integral quantities relative to the next refinement level were below approximately 0.5%. These results indicate that M2 provides sufficient resolution for the surface-integrated heat flux and Nusselt number over the investigated shape space.

[2] In our previous work [20,27], a boundary element method (BEM) was employed for Stokes-flow calculations around superellipsoidal particles. BEM is an efficient tool for solving tractions at the particle surface. However, in the current case where coupling with heat transfer is required, the velocity field throughout the domain is necessary. This necessitates creating a domain mesh and evaluating velocity at the nodes of this mesh using an explicit BEM calculation. The explicit BEM calculation necessitates evaluating boundary integrals over the surface of the particle for each domain node. This is a highly time-consuming step, which counteracts the primary advantage of BEM—namely, avoiding domain discretization. Our computational tests showed that the BEM approach becomes substantially more expensive, whereas the finite-volume formulation implemented in OpenFOAM provides a more efficient framework for generating the large DNS database considered here. We therefore adopted the OpenFOAM-based approach for the present study.

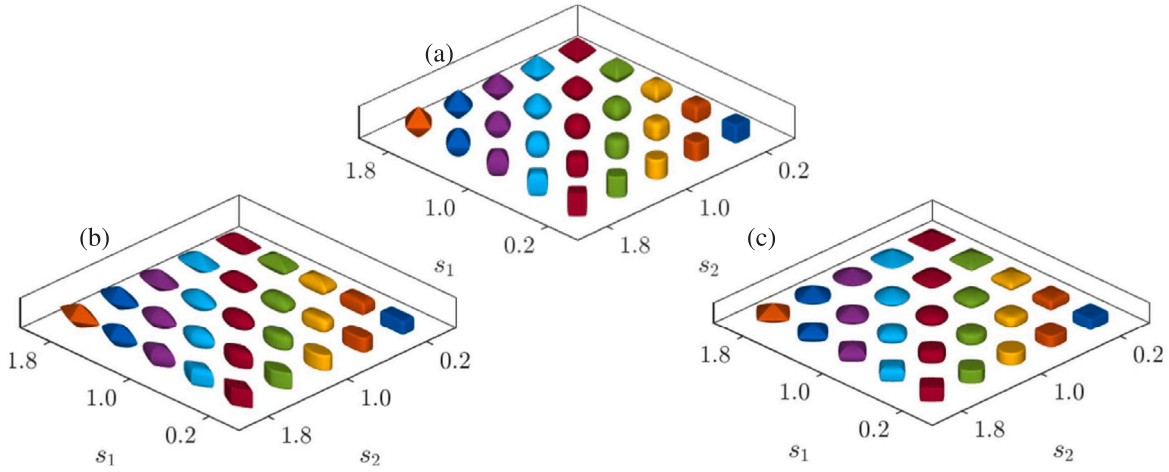


Fig. 2. A set of superellipsoidal shapes for (a) $\lambda_1 = \lambda_2 = 1$ (isotropic), (b) $\lambda_1 = 2$ $\lambda_2 = 1$ (prolate) and (c) $\lambda_1 = \lambda_2 = 2$ (oblate) with varying $s_1, s_2 \in [0.2, 1.8]$.

3. Non-spherical particles of superellipsoidal shape

In order to include a wide variety of different particle shapes we model non-spherical particles as superellipsoids. A superellipsoidal shape is described by a parametric surface, [28,29], defined in the particle-frame-of-reference by

$$S(x_1, x_2, x_3) = \left[\left[\frac{x_1}{a_1} \right]^{2/s_2} + \left[\frac{x_2}{a_2} \right]^{2/s_2} \right]^{s_2/s_1} + \left[\frac{x_3}{a_3} \right]^{2/s_1} . \tag{23}$$

Fixing the volume to $V = \pi/6$, that is, to the volume of an equivalent sphere with $d_{\mathrm{eq}} = 1$ (assumed throughout in the sequel), we can express the three semi-axes a_1, a_2, a_3 as

$$a_1 = \lambda_1 a_3, \qquad a_2 = \lambda_2 a_3,$$
$$a_3 = \left[\frac{\pi}{12\, \lambda_1 \lambda_2 s_1 s_2 B(s_1/2, s_1 + 1) B(s_2/2, [s_2 + 2]/2)} \right]^{1/3} , \tag{24}$$

where λ_1, λ_2 are the aspect ratios and $B(\bullet, \circ)$ is the beta function. Thus, for $V = \pi/6$, the superellipsoidal shape is defined by only four parameters, that is, the aspect ratios λ_1, λ_2 and the shape exponents s_1, s_2.

We denote shapes with $\lambda_1 = \lambda_2 = 1$ as *isotropic* and with $\lambda_1, \lambda_2 \neq 1$ as *anisotropic*. Specifically, $\lambda_1 = \lambda_2 > 1$ characterize *oblate* and $\lambda_1 > \lambda_2$ *prolate* shapes. Furthermore, we denote shapes with $s_1 = s_2$ as *symmetric* and with $s_1 \neq s_2$ as *asymmetric*. Specifically, $s_1 = s_2 = 1$ describe *ellipsoidal*, $s_1 = s_2 < 1$ *cubical*, and $s_1 = s_2 > 1$ *diamond* shapes.

For our subsequent evaluations of the heat flux q_{n} and its resultant, the surface area of the particle is also required. In contrast to volume, no closed-form expression is available for the surface area of a superellipsoid. Therefore, we evaluate the surface area numerically based on the discretized surface of the particle as generated in OpenFOAM. In continuous form, the surface area is given by $A := \int_\Gamma \mathrm{d}A$. In the numerical implementation, this integral is approximated by summing over all surface facets of the discretized particle surface, $A^h \approx \sum_i A_f$, where A^h denotes the discretized particle surface, with h indicating the discretization size, and A_f the area of the surface facet f.

A set of superellipsoidal particles with fixed λ_1, λ_2 and for varying s_1, s_2 is presented in Fig. 2, highlighting the wide range of shapes that can be generated using superellipsoids.

4. Orientation dependence of the nusselt number

First, we investigate the orientation dependence of Nu when varying $\mathrm{Pe} = U\, d_{\mathrm{eq}}/\alpha^{\mathrm{f}}$ (for $d_{\mathrm{eq}} = 1$) by studying whether the orientation of a particle relative to the surrounding flow influences its convective heat transfer. For this purpose, the following representative superellipsoidal particles are considered: ellipsoidal ($s_1 = s_2 = 1$), cubical ($s_1 = s_2 = 0.2$), and diamond ($s_1 = s_2 = 1.8$) shapes of prolate or oblate character with $\lambda_1 = [2.5, 5, 7.5]$ and $\lambda_2 = [1, \lambda_1]$.

The orientational dependence of Nu is examined by exposing the particles to various ambient flow fields $\boldsymbol{u} = \boldsymbol{v}_{\mathrm{f}}^{\infty} - \boldsymbol{v}_{\mathrm{s}}$ (with $\boldsymbol{v}_{\mathrm{s}}$ here set to zero without loss of generality). Here, the imposed relative velocity $\underline{u}$ is aligned with one of seven directions in the particle principal-coordinate system: the three principal axes $\underline{u}_x$, $\underline{u}_y$, and $\underline{u}_z$; the three principal-plane diagonals $\underline{u}_{xy}$, $\underline{u}_{xz}$, and $\underline{u}_{yz}$; or the space diagonal $\underline{u}_{xyz}$. These directions are defined as

$$\underline{u}_x = U\,[1,0,0], \quad \underline{u}_y = U\,[0,1,0], \quad \underline{u}_z = U\,[0,0,1],$$
$$\underline{u}_{xy} = \frac{U}{\sqrt{2}}[1,1,0], \quad \underline{u}_{xz} = \frac{U}{\sqrt{2}}[1,0,1], \quad \underline{u}_{yz} = \frac{U}{\sqrt{2}}[0,1,1], \quad \underline{u}_{xyz} = \frac{U}{\sqrt{3}}[1,1,1].$$

To quantify the significance of orientational effects, we evaluate the coefficient of variation, CV, of Nu across these seven flow fields. The coefficient of variation allows us to identify regimes in which the influence of particle orientation on convective heat transfer becomes non-negligible. It is defined as the ratio between the standard deviation of Nu across all orientations considered and its corresponding mean value $\overline{\mathrm{Nu}}$, which expands as

$$\mathrm{CV} = \frac{\sqrt{\frac{1}{N} \sum_{i=1}^{N} \left[\mathrm{Nu}_i - \overline{\mathrm{Nu}} \right]^2}}{\overline{\mathrm{Nu}}} , \tag{25}$$

where $N = 7$ is the number of sample orientations and Nu_i denotes the Nusselt number corresponding to the ith orientation of the flow field.

Fig. 3 illustrates CV as a function of Pe for the various particle shapes considered. For all shapes, CV remains negligibly small for $\mathrm{Pe} < 1$, indicating that the orientation of the particle relative to the flow has no measurable influence on the convective heat transfer in this regime. This behavior reflects the dominance of diffusive transport at low Pe, for which convective effects, and thus orientation-dependent flow features, are insignificant.

In contrast, for $\mathrm{Pe} > 1$ the coefficient of variation increases monotonically, demonstrating a growing influence of particle orientation on convective heat transfer. As convection becomes increasingly important, the interaction between the flow field and the particle shape leads to orientation-dependent variations in local heat flux, which are captured by an increasing spread in Nu, that is, an increase in CV. As Re_{p} is well below 1, the case of $\mathrm{Pe} > 1$ corresponds to cases of fluids with high Pr number values.

Furthermore, we find that the magnitude of the orientation dependence strongly depends on the particle shape. The cubical particles studied exhibit the smallest CV throughout the range of Pe, indicating

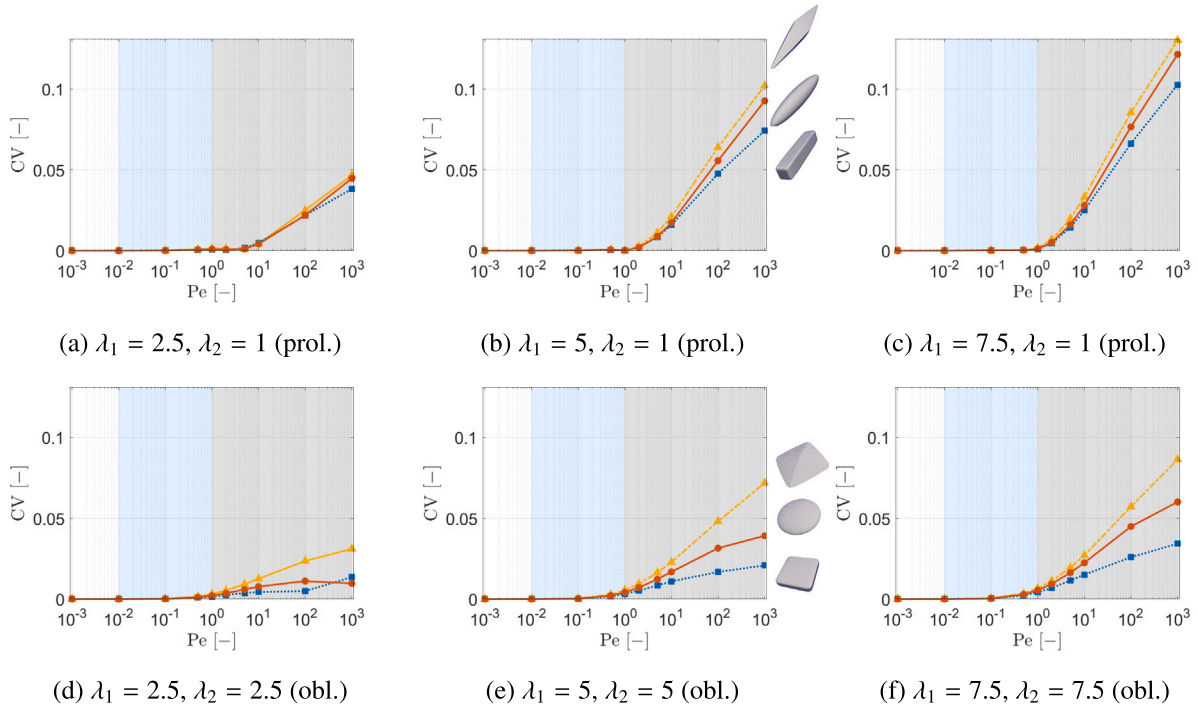


Fig. 3. Coefficient of variation, CV, of Nu for ellipsoidal, cubical and diamond shapes of prolate and oblate character as function of Pe. Particles (a–c) with $\lambda_1 = 2.5, 5, 7.5$ and $\lambda_2 = 1$ (prolate particles), and (d–f) with $\lambda_1 = 2.5, 5, 7.5$ and $\lambda_2 = \lambda_1$ (oblate particles). Results arranged from top to bottom in the diagrams: $s_1 = s_2 = 1.8$ (diamond), $s_1 = s_2 = 1.0$ (ellipsoidal), and $s_1 = s_2 = 0.2$ (cubical).

a comparatively smaller local variation in convective heat transfer. In contrast, ellipsoidal and diamond shapes show a significantly stronger orientation dependence, with diamond shapes possessing the highest sensitivity to orientation. Note that the purpose of Fig. 3 is to identify the onset and magnitude of orientation dependence rather than to compare the absolute values of Nu. The coefficient of variation therefore provides a compact measure of the relative spread of Nu over the considered orientations. The complete orientation-resolved Nusselt-number data are available in the accompanying Zenodo repository [30].

To further illustrate the origin of the observed orientation dependence, we also examined the spatial distribution of the local heat flux q_n over the particle surface. While Nu provides a surface-averaged global measure of convective heat transfer, the local heat flux reveals in more detail how particle orientation affects its distribution. Fig. 4 shows the surface heat-flux magnitude for selected prolate particle shapes and flow orientations at Pe = 1. Here, the distribution of heat flux remains nearly agnostic to the particle orientation, consistent with diffusion-dominated heat transfer and the negligible orientation dependence observed in Nu.

In contrast, at Pe = 100, pronounced spatial variations in heat flux emerge, see Fig. 5. As observed, regions facing the incoming flow exhibit significantly enhanced heat flux, while leeward regions experience reduced heat flux. Furthermore, we find that these effects are strongly shape-dependent. The spatial distribution of local heat flux q_n clearly explains the increased CV of Nu observed for particles at higher Pe.

The increase in the coefficient of variation for Pe > 1 also marks the limit of applicability of an orientation-independent surrogate model. In this regime, the relative-flow direction in the particle frame becomes an additional relevant input, and a model depending only on particle shape and Pe is no longer sufficient. Accordingly, the surrogate models developed below are restricted to Pe ≤ 1, where the orientation dependence remains negligible over the investigated shape space. Extension to Pe > 1 would require an orientation-resolved DNS database and an orientation-aware surrogate formulation, which are beyond the scope of the present study.

5. Shape dependence of the nusselt number

In the sequel, the analysis and surrogate-model development are restricted to Pe ≤ 1. This range was deliberately chosen because the orientation dependence of Nu is negligible over the investigated particle-shape space, thereby allowing the construction of a compact orientation-independent closure. The restriction is consistent with the intended application within the Stokes-regime point-particle framework used in our previous studies [20,21].

Simulations were conducted for 1125 (45x5x5) distinct superellipsoidal particle shapes. The shape space spans $(9\times9)^{\mathrm{sym}} = 45$ aspect ratios $\lambda_1, \lambda_2 \in [1, 9]$ ($\lambda_2 \le \lambda_1$) and 5×5 shape exponents $s_1, s_2 \in [0.2, 1.8]$. In addition, seven Péclet numbers in the range Pe ∈ [0.001, 1.0] were considered, resulting in a total of 7875 (45x5x5x7x1) DNS simulations.

In the following, we analyze the shape dependence of Nu by systematically varying the aspect ratios λ_1, λ_2 and the shape exponents s_1, s_2, and plot the corresponding surfaces $\mathrm{Nu} = \mathrm{Nu}(\lambda_1, \lambda_2; \mathrm{Pe})|_{s_1,s_2}$ and $\mathrm{Nu} = \mathrm{Nu}(s_1, s_2; \mathrm{Pe})|_{\lambda_1,\lambda_2}$ at various Pe. The smoothness of the resulting surfaces suggests that the data sampling density with 7875 DNS simulations is sufficiently accurate.

5.1. Varying the aspect ratios λ_1, λ_2

Fig. 6 shows the variation of $\mathrm{Nu} = \mathrm{Nu}(\lambda_1, \lambda_2; \mathrm{Pe})|_{s_1,s_2}$ as a function of the aspect ratios λ_1, λ_2 for different shape exponents s_1, s_2 at various Péclet numbers Pe. The lower values ($s_1 = s_2 = 0.2$) of the shape exponents correspond to more cubical shapes and the higher values ($s_1 = s_2 = 1.8$) to more diamond shapes. Figs. 6(a)–(c) present symmetric shapes with $s_1 = s_2$, while (d) corresponds to an asymmetric superellipsoid with $s_1 \neq s_2$.

For all s_1, s_2 and Pe considered, Nu decreases monotonically with increasing λ_1, λ_2. This trend is consistently observed throughout the

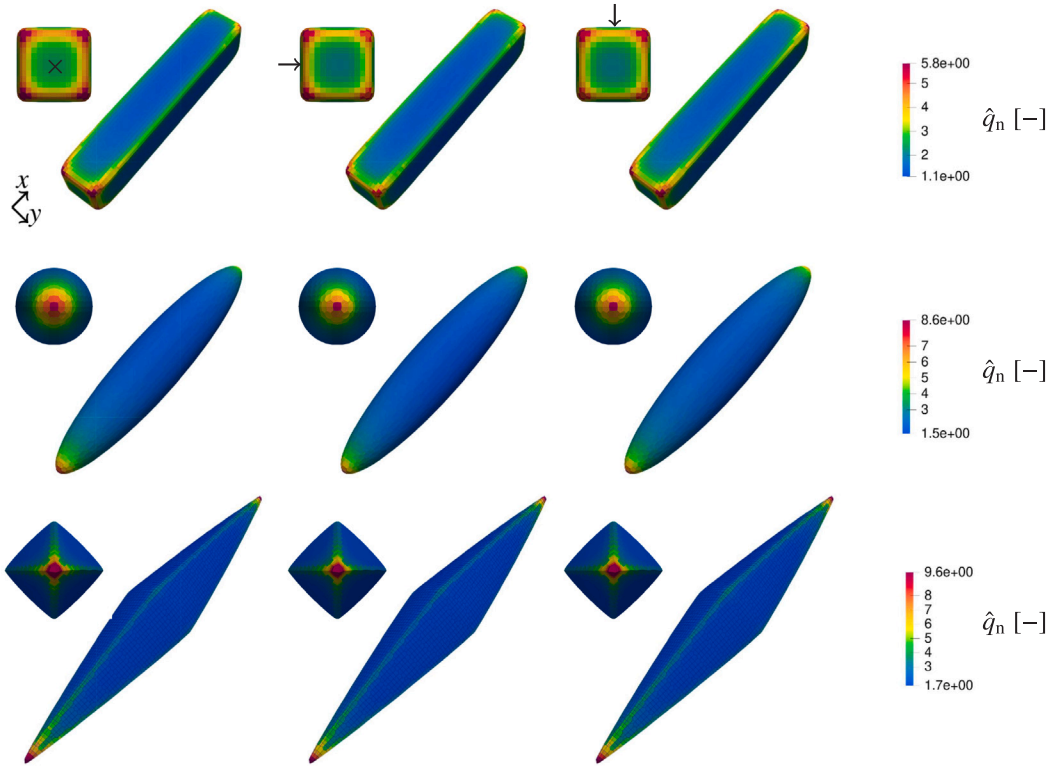


Fig. 4. Normalized local heat flux $\hat{q}_n = q_n d_{eq}/[k^f \Delta T]$ on prolate superellipsoidal particles in different flow fields at Pe = 1 : (Left) $\underline{u}_x$, (Middle) $\underline{u}_y$, (Right) $\underline{u}_z$. Resulting Nu for the specified shape (λ_1, λ_2, s_1, s_2): cube (5,1,0.2,0.2) 2.01547 (left), 2.01546 (middle), 2.01546 (right), ellipsoid (5,1,1,1) 2.1376 (left), 2.13644 (middle), 2.13645 (right), diamond (5,1,1.8,1.8) 2.05423 (left), 2.05362 (middle), 2.05363 (right).

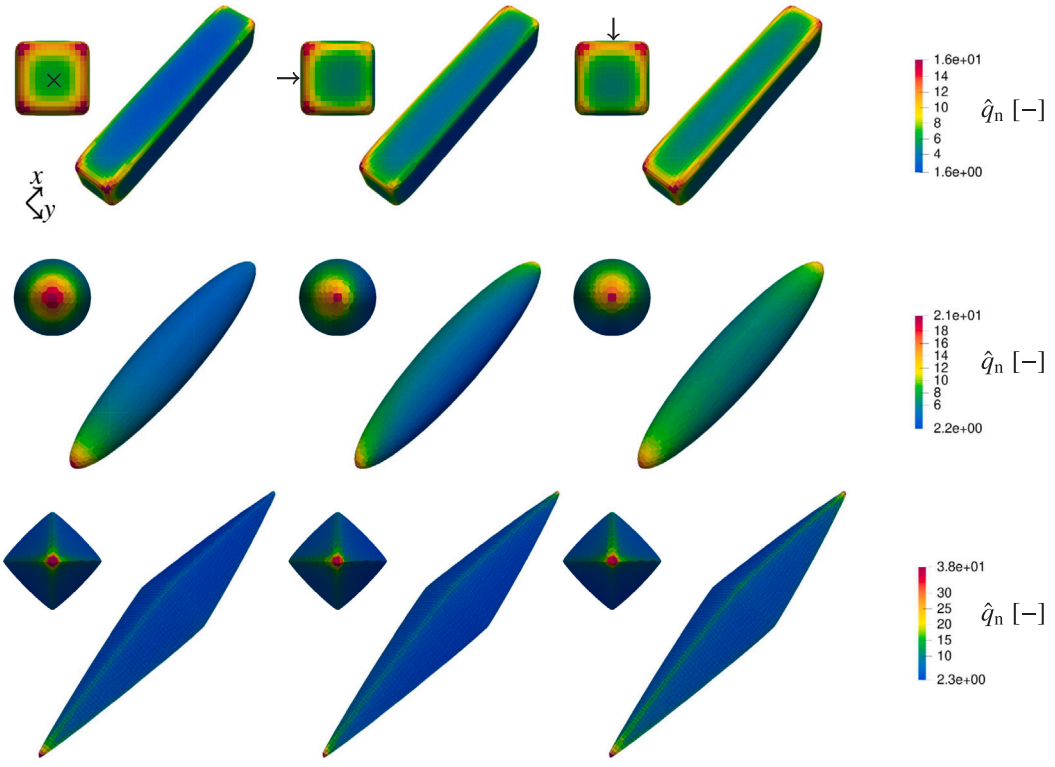


Fig. 5. Normalized local heat flux $\hat{q}_n = q_n d_{eq}/[k^f \Delta T]$ on prolate superellipsoidal particles in different flow fields at Pe = 100 : (Left) $\underline{u}_x$, (Middle) $\underline{u}_y$, (Right) $\underline{u}_z$. Resulting Nu for the specified shape (λ_1, λ_2, s_1, s_2): cube (5,1,0.2,0.2) 4.63989 (left), 5.30022 (middle), 5.30040 (right), ellipsoid (5,1,1,1) 4.8652 (left), 5.70288 (middle), 5.70319 (right), diamond (5,1,1.8,1.8) 4.58753 (left), 5.5324 (middle), 5.53302 (right). .

Table 1
Distinct convective heat transfer regimes based on the Péclet number.

Péclet number range	Model dependence
$Pe \leq 0.01$	$Nu = f(\text{shape})$
$0.01 < Pe \leq 1$	$Nu = f(\text{shape}, Pe)$
$Pe > 1$	$Nu = f(\text{shape}, Pe, \text{orientation})$

Table 2
Minimum and maximum DNS Nusselt numbers at the investigated Péclet numbers. The corresponding particle shape is specified by $(\lambda_1, \lambda_2, s_1, s_2)$.

Pe	Nu_{min}	Shape at Nu_{min}	Nu_{max}	Shape at Nu_{max}
0.001	1.00396	(9, 9, 1.8, 0.2)	1.988400	(1, 1, 1, 1)
0.01	1.00733	(9, 9, 1.8, 0.2)	1.992310	(1, 1, 1, 1)
0.1	1.04012	(9, 9, 1.8, 0.2)	2.032050	(1, 1, 1, 1)
0.25	1.08423	(9, 9, 1.8, 0.2)	2.088060	(1, 1, 1, 1)
0.5	1.14289	(9, 9, 1.8, 0.2)	2.165540	(1, 1, 1, 1)
0.75	1.19104	(9, 9, 1.8, 0.2)	2.231030	(1, 1, 1, 1)
1	1.23255	(9, 9, 1.8, 0.2)	2.288580	(1, 1, 1, 1)

entire range of Pe and reflects the reduced convective heat transfer for particles with more anisotropic shape, for which the characteristic diffusion length increases and the local thermal gradients weaken.

The discernible influence of Pe is evident for all shapes. At higher Pe, convection improves heat transfer, leading to larger Nu and a clear separation between the results corresponding to different Pe. However, as Pe decreases, Nu and its sensitivity to Pe also decrease. In particular, the $Nu = Nu(\lambda_1, \lambda_2; Pe)|_{s_1,s_2}$ surfaces at $Pe = 0.01$ and $Pe = 0.001$ nearly collapse for all combinations of s_1, s_2 and λ_1, λ_2, indicating a diffusion-dominated regime in which further reductions in Pe have a negligible effect on convective heat transfer.

This observation enables the definition of distinct convective heat transfer regimes (see Table 1): for $Pe \leq 0.01$, Nu becomes independent of Pe and depends only on particle shape; for $0.01 < Pe \leq 1$, the dependence on Pe must be retained additionally; while for $Pe > 1$, the shape, Pe and particle orientation are expected to play a significant role. These regimes are highlighted in Fig. 3.

Beyond these general trends, Fig. 6 highlights a pronounced dependence of Nu on s_1, s_2. For comparable λ_1, λ_2 and Pe, cubical shapes ($s_1 = s_2 = 0.2$) consistently exhibit higher Nu than diamond shapes ($s_1 = s_2 = 1.8$). This behavior can be attributed to the presence of flatter faces for cubical shapes, which promote stronger local thermal gradients compared to smoother, more pointed shapes.

The symmetric cases ($s_1 = s_2$) exhibit smooth and nearly monotonic variations of Nu with λ_1, λ_2, while the asymmetric case ($s_1 = 0.2$, $s_2 = 1.8$) shows a more complex response. Here, the combined effects of λ_1, λ_2 and asymmetric surface curvature lead to Nu values intermediate to those of symmetric cubical and diamond shapes, emphasizing the role of shape asymmetry in particle-scale heat transfer.

In summary, Fig. 6 clearly demonstrates that Nu is governed by a coupled dependence on the four parameters λ_1, λ_2, s_1, s_2 of a superellipsoidal shape, and Pe.

Fig. 6 illustrates representative variations of Nu with λ_1 and λ_2 for selected combinations of s_1 and s_2. For completeness, Table 2 summarizes the corresponding extrema across the full sampled parameter space. Within the sampled shape space, the smallest Nu is obtained for $(\lambda_1, \lambda_2, s_1, s_2) = (9, 9, 1.8, 0.2)$, while the largest value is obtained for the spherical particle $(1, 1, 1, 1)$ at every investigated Pe. Note that both extrema increase monotonically with increasing Pe. Across the complete sampled parameter space, the obtained Nu values span approximately $1.004 \leq Nu \leq 2.289$.

5.2. Varying the shape exponents s_1, s_2

Fig. 7 shows the variation of $Nu = Nu(s_1, s_2; Pe)|_{\lambda_1,\lambda_2}$ as a function of the shape exponents s_1, s_2 for different aspect ratios λ_1, λ_2 at various Péclet numbers Pe. Panels (a)–(d) correspond to progressively increasing aspect ratios, ranging from isotropic shapes ($\lambda_1 = \lambda_2 = 1$) to highly oblate shapes ($\lambda_1 = \lambda_2 = 7$), with results shown at multiple values of Pe.

For fixed aspect ratios, variations in shape exponents lead to noticeable changes in Nu. Although these variations are generally smaller than those induced by changes in λ_1, λ_2, the influence of s_1, s_2 remains significant, with differences that extend to approximately 35% when comparing the resulting Nu for $s_1 = 0.2, s_2 = 1.8$ with that for $s_1 = 1.8, s_2 = 0.2$ at $\lambda_1 = \lambda_2 = 7$ and $Pe = 1$. This clearly highlights that shape exponents play an important role in determining the convective heat transfer coefficient of micron-sized particles in addition to their aspect ratios, thus rendering a simple ellipsoidal approximation insufficient for an accurate prediction of Nu.

An important observation is that the sensitivity of $Nu = Nu(s_1, s_2; Pe)|_{\lambda_1,\lambda_2}$ to shape exponents increases with aspect ratios. Isotropic shapes ($\lambda_1 = \lambda_2 = 1$) exhibit relatively modest variations with s_1, s_2, whereas particles with higher aspect ratios show steeper gradients when varying s_1, s_2. This indicates a coupling between aspect ratios and surface curvature effects, whereby shape exponent-induced differences in local thermal gradients are amplified for slender geometries.

The influence of Pe remains consistent throughout all superellipsoidal shapes. Higher Pe produce uniformly larger Nu, while decreasing Pe leads to a collapse of the surfaces $Nu = Nu(s_1, s_2; Pe)|_{\lambda_1,\lambda_2}$, particularly between $Pe = 0.01$ and $Pe = 0.001$. Note that the relative ranking of $Nu(s_1, s_2; Pe)|_{\lambda_1,\lambda_2}$ is preserved throughout all Pe, indicating that the variation of Nu with s_1, s_2 is largely independent of the $Pe \leq 1$ regime.

While the Nusselt number characterizes the normalized heat-transfer coefficient, it does not directly quantify the total amount of heat transferred by the particle. Thus, for completeness, we provide an analysis of the total thermal power exchanged between the particle and the surrounding fluid in Appendix C

6. Surrogate modeling

The surrogate models developed in this section are restricted to the investigated low-Peclet-number range, $Pe \leq 1$. In the above we found that the resulting Nusselt number strongly depends on the aspect ratios λ_1, λ_2 and the shape exponents s_1, s_2. Thus, to characterize the convective heat transfer of superellipsoidal particles in flow, both a Nusselt number *correlation* and a *physics-constrained neural network* model were developed to predict the Nusselt number as a function of particle shape $(\lambda_1, \lambda_2, s_1, s_2)$ and flow conditions (Pe). The objective of these models is to learn the nonlinear mapping between the set of five governing parameters (four superellipsoidal shape parameters contained in $\boldsymbol{\xi} := [\lambda_1, \lambda_2, s_1, s_2]$ and the Péclet number Pe) and the resulting Nusselt number.

6.1. Nusselt number correlation model

First, we develop a Nusselt number correlation model that embeds a known physical structure, including correct low Péclet number behavior and constrained scaling with the Péclet number. This formulation yields a compact model that allows for physical interpretation and improves stability outside the training range..

6.1.1. Model formulation

The Nusselt number is represented as a diffusion-dominated baseline contribution (Nu_0) multiplied by a convective enhancement factor,

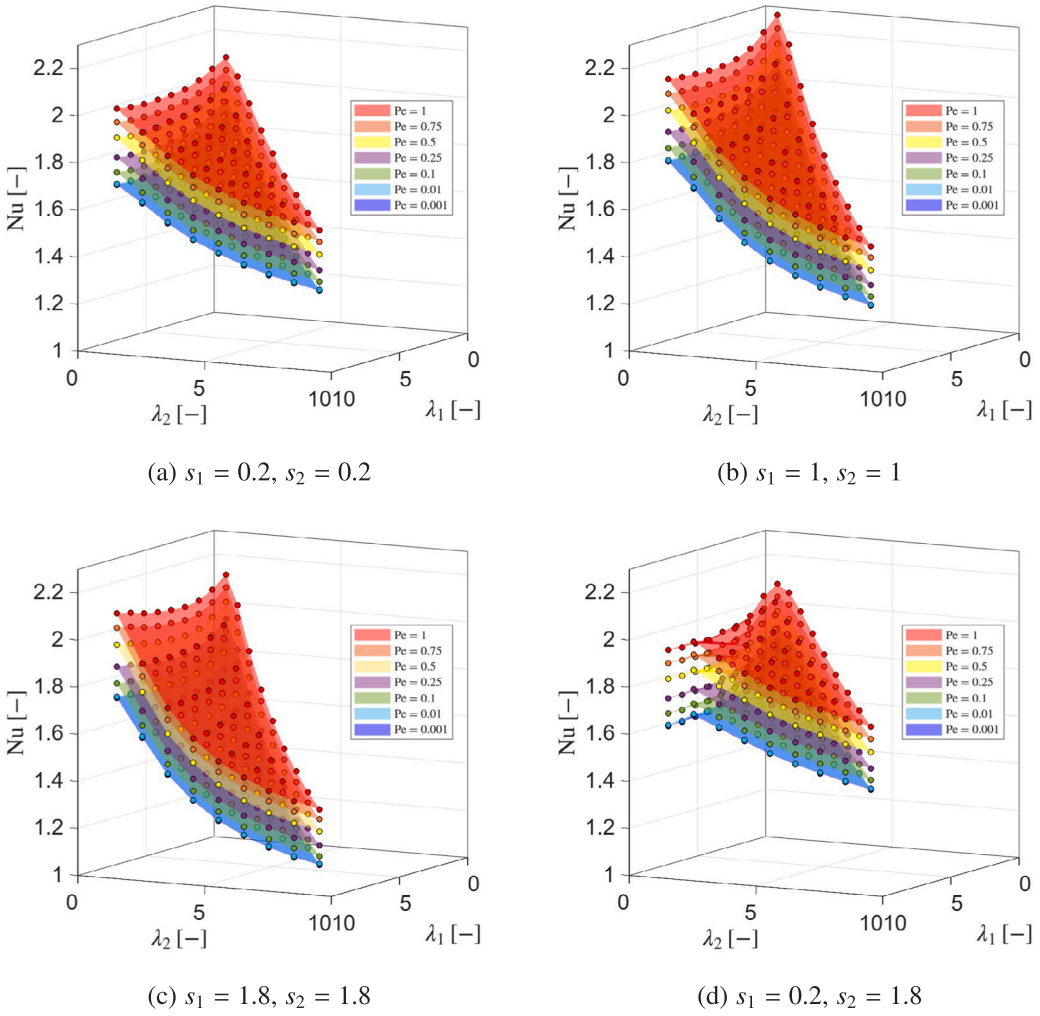


Fig. 6. Nusselt number for superellipsoidal particles with fixed s_1, s_2 for varying aspect ratios λ_1, λ_2 at different Pe.

$$\mathrm{Nu}(\boldsymbol{\xi}, \mathrm{Pe}) = \mathrm{Nu}_0(\boldsymbol{\xi})\,[1 + g(\boldsymbol{\xi}, \mathrm{Pe})] \quad \text{with} \quad g(\boldsymbol{\xi}, \mathrm{Pe}) = \underbrace{\mathrm{Pe}^m \exp\big(\eta_1(\boldsymbol{\xi})\big) + \mathrm{Pe}^n \exp\big(\eta_2(\boldsymbol{\xi})\big)}_{\text{convective enhancement}}. \tag{26}$$

The baseline term Nu_0 represents the diffusion-controlled limit, while the bracketed expression describes the relative convective enhancement of heat transfer. This multiplicative separation is advantageous from a modeling and implementation perspective, as it allows the diffusion-dominated contribution $\mathrm{Nu}_0(\boldsymbol{\xi})$ to be treated independently, effectively yielding a standalone model for regimes with $\mathrm{Pe} \leq 0.01$, where convective effects are negligible.

This multiplicative structure corresponds to modeling convection as a shape- and Péclet number-dependent amplification of the diffusion-controlled baseline, rather than as a fixed absolute increment. Such a formulation is particularly suitable when the convective contribution scales approximately with the magnitude of the baseline heat transfer. The choice of two Pe exponents is motivated in Appendix D.

6.1.2. Shape basis functions

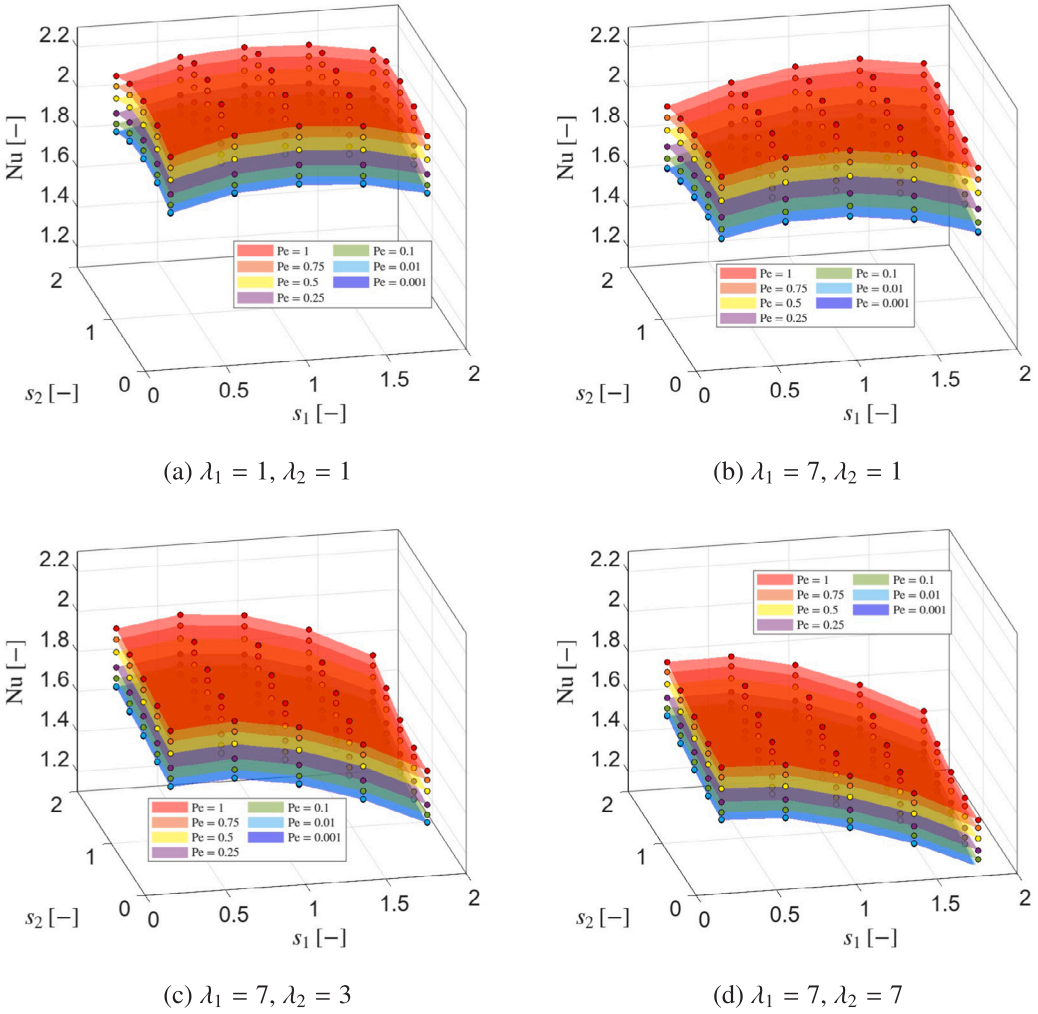
The shape dependence of Nu_0, η_1, and η_2 is expressed as linear combinations of engineered basis functions,

$$\mathrm{Nu}_0(\boldsymbol{\xi}) = \sum_i a_i \, \Phi_i^0(\boldsymbol{\xi}), \qquad \eta_k(\boldsymbol{\xi}) = \sum_j b_{k,j} \, \Phi_j^{\eta_k}(\boldsymbol{\xi}), \quad k = 1, 2. \tag{27}$$

The basis functions are constructed to capture the impact of geometric features on Nu through:

1. Elongation and anisotropy: Overall particle elongation and directional anisotropy are described using $E_1 := \log(\lambda_1 \lambda_2)$ and $E_2 := \lambda_1/\lambda_2$, which characterize isotropic elongation and directional aspect-ratio effects, respectively.
2. Shape exponent deviations: Shape exponents are referenced relative to the spherical (and ellipsoidal) state, $S_1 := s_1 - 1$, $S_2 := s_2 - 1$, allowing both linear and nonlinear deviations from the reference geometry to be represented. The parameters S_1 and S_2 are treated independently, as the governing physics is not invariant under interchange of s_1 and s_2.
3. Polynomial and interaction terms: The basis includes linear, quadratic, and cubic terms in S_1 and S_2, mixed interaction terms such as $S_1 S_2$, and coupling terms between elongation and shape exponent deviations, e.g. $E_1 S_i$, $E_2 S_i$, $E_1 S_i^2$, and $E_2 S_i^2$. These interaction terms allow the sensitivity of both the diffusion baseline and the convective enhancement to vary systematically with particle elongation and anisotropy.

A reduced but consistent subset of these basis functions is employed for η_1 and η_2, reflecting the observation that the convective enhancement amplitudes require fewer high-order terms than the baseline contribution.



(a) $\lambda_1 = 1, \lambda_2 = 1$ (b) $\lambda_1 = 7, \lambda_2 = 1$

(c) $\lambda_1 = 7, \lambda_2 = 3$ (d) $\lambda_1 = 7, \lambda_2 = 7$

Fig. 7. Nusselt number for superellipsoidal particles with fixed λ_1, λ_2 for varying shape exponents s_1, s_2 at different Pe.

6.1.3. *Enforced physical constraints*

Several physical constraints are enforced directly in the model formulation:

1. Correct diffusion limit: Since $m > 0$ and $n > m$, both convective terms vanish as $\mathrm{Pe} \to 0$, and the multiplicative factor approaches unity, ensuring $\lim_{\mathrm{Pe}\to 0} \mathrm{Nu}(\boldsymbol{\xi}, \mathrm{Pe}) = \mathrm{Nu}_0(\boldsymbol{\xi})$.
2. Positivity of the Nusselt number: The diffusion baseline Nu_0 is constrained to be positive, and the exponential parametrization $\exp(\eta_k(\boldsymbol{\xi}))$ $(k = 1, 2)$ guarantees that the convective enhancement factor is strictly non-negative for all particle shapes.
3. Ordered Péclet number scaling: The exponents are constrained such that $m > 0$, $n > m$;
   enforced via a SoftPlus ($\mathrm{Softplus}(z) = \ln(1 + e^z)$) reparameterization during training. This prevents collapse to a single effective power law and enforces two distinct Péclet number scalings.
4. Smooth regime transition: The combined enhancement factor $1 + \mathrm{Pe}^m \exp(\eta_1(\boldsymbol{\xi})) + \mathrm{Pe}^n \exp(\eta_2(\boldsymbol{\xi}))$, allows the effective Péclet number dependence to transition smoothly between regimes dominated by the lower or higher exponent, depending on Pe and particle shape.

For the spherical configuration, $\boldsymbol{\xi}_{\mathrm{sph}} = (1, 1, 1, 1)$, the exact pure-conduction limit is $\mathrm{Nu} = 2$ as $\mathrm{Pe} \to 0$. In the present formulation, however, the baseline Nu_0 is identified from the DNS data at the smallest sampled value, $\mathrm{Pe}_{\mathrm{ref}} = 0.001$, rather than at $\mathrm{Pe} = 0$. The corresponding spherical DNS value differs slightly from 2 owing to numerical discretization and finite-domain effects. Therefore, $\mathrm{Nu}_0(\boldsymbol{\xi}_{\mathrm{sph}}) = 2$ is not imposed exactly during fitting. Enforcing this value while retaining the non-negative convective-enhancement constraint, $\mathrm{Nu} \geq \mathrm{Nu}_0$, would prevent the model from reproducing a finite-Pe DNS value below 2 and would consequently require either a reformulation of the baseline or a relaxation of this constraint.

For the spherical configuration, the low-Pe dependence is additionally assessed against the asymptotic solution of Acrivos and Taylor [31], see Appendix B.1.2. This relation is used as an independent consistency check rather than as an additional fitting constraint

6.1.4. *Parameter estimation*

All coefficients and exponent parameters are determined by minimizing the mean-squared error between the predicted and reference Nusselt numbers. The optimization is performed using the gradient-based AdamW [32,33] algorithm. The parameter-identification procedure is carried out in two stages. First, the coefficients of the baseline contribution Nu_0 are fitted using the data at $\mathrm{Pe} = 0.001$. The resulting baseline model is then held fixed, while the coefficients of the two Péclet-dependent enhancement terms, together with the exponent parameters m and n, are fitted simultaneously using the complete DNS

dataset. The corresponding objective function is

$$\mathcal{L}(\boldsymbol{\theta}) = \frac{1}{N}\sum_{i=1}^{N}\left[\mathrm{Nu}_{\mathrm{corr}}\left(\lambda_1^i, \lambda_2^i, s_1^i, s_2^i, \mathrm{Pe}^i; \boldsymbol{\theta}\right) - \mathrm{Nu}_{\mathrm{DNS}}^i\right]^2, \tag{28}$$

where $\boldsymbol{\theta}$ collects all fitted coefficients and exponent parameters. To obtain a compact and interpretable correlation, the candidate basis functions are subsequently reduced through iterative backward pruning. At each pruning step, the term with the smallest coefficient-weighted root-mean-square contribution is removed and the remaining parameters are reoptimized. A reduced basis is accepted when the resulting decrease in the coefficient of determination does not exceed 5×10^{-4}. No additional Pe-dependent basis functions beyond the prescribed power-law structure are introduced.

After systematic pruning, the final basis sets for the enhancement $\boldsymbol{\Phi}^{\eta_k}$ and the baseline model $\boldsymbol{\Phi}^0$ were chosen as

$$\boldsymbol{\Phi}^{\eta_1} = \left\{1, E_1, E_1^2, E_1^3, E_2, E_1^3 S_1\right\},$$
$$\boldsymbol{\Phi}^{\eta_2} = \left\{1, E_1, E_1^2, E_1^3, E_2, E_2^3, E_1^2 E_2, E_1^3 S_1, E_1^3 S_2, E_2^3 S_1\right\}$$

and

$$\begin{aligned}\boldsymbol{\Phi}^0 = \{&1,\ E_1,\ E_1^2,\ E_1^3,\ E_2,\ E_2^2,\ E_2^3,\ E_1E_2,\ E_1^2E_2,\ E_1E_2^2,\ S_1^2,\ S_2^2,\\ &E_1S_1,\ E_2S_1,\ E_2S_1S_2,\ E_1^2S_1,\ E_1^2S_2,\ E_1^3S_1,\ E_1^3S_2,\ E_2^2S_1,\\ &E_2^2S_2,\ E_2^3S_1,\ E_2^3S_2,\ E_1S_2^2,\ E_1S_1^3\ \}.\end{aligned}$$

This analytical structure enforces the correct asymptotic behavior for $\mathrm{Pe}\to 0$ and guarantees positivity of the enhancement terms through the exponential representation. The resulting surrogate remains fully interpretable, with each term corresponding to a clear geometric interaction. The resulting coefficients are provided in Appendix E.

6.1.5. Results: Nusselt number correlation model

In this section, the performance of the proposed Nusselt number correlation model is evaluated. All available DNS data were used for parameter identification and basis-function pruning. The model was fitted by minimizing the normalized mean-squared error

$$\mathrm{NMSE} = \frac{1}{N}\sum_{i=1}^{N}\frac{\left[\mathrm{Nu}_i^{\mathrm{DNS}} - \mathrm{Nu}_i^{\mathrm{CM}}\right]^2}{\left[\mathrm{Nu}_i^{\mathrm{DNS}}\right]^2}, \tag{29}$$

which weighs errors relative to the magnitude of the Nusselt number and prevents large values from dominating the optimization. The model achieves a NMSE $= 3.667\times 10^{-5}$ with coefficient of correlation $R^2 = 0.9982$ over the complete database.

The reported errors are evaluated using the same DNS database employed for parameter identification and therefore quantify the interpolation accuracy of the correlation over the sampled parameter domain rather than its generalization error on an independent test set. The risk of overfitting is limited by the strongly overdetermined regression problem, with only 43 fitted parameters for 7875 DNS samples, by the prescribed low-order Péclet-number dependence, and by the systematic pruning of the candidate basis. These results demonstrate that the proposed correlation accurately reproduces the DNS data throughout the sampled parameter domain.

Fig. 8(a) shows the predicted Nusselt number plotted against the corresponding measured values for the full dataset. The data points collapse tightly along the identity line ($\mathrm{Nu}_{\mathrm{CM}} = \mathrm{Nu}_{\mathrm{DNS}}$), confirming the absence of systematic bias. The small scatter around the diagonal reflects the very high coefficient of determination ($R^2 \approx 0.9982$).

Furthermore, Fig. 8(b) displays the relative error

$$\epsilon_{\mathrm{rel}} = \frac{\mathrm{Nu}_{\mathrm{CM}} - \mathrm{Nu}_{\mathrm{DNS}}}{\mathrm{Nu}_{\mathrm{DNS}}} \tag{30}$$

as a function of the measured Nusselt number. As observed, the vast majority of data points lie within the $\pm 1\%$ bounds. The absence of clearly structured residual patterns indicates that the correlation reproduces the principal trends of the DNS database consistently throughout the sampled parameter range. The maximum observed deviation remains below 2.5%, demonstrating that the imposed physical constraints do not reduce predictive flexibility but instead stabilize and regularize the regression problem.

6.2. Nusselt number physics-constrained neural network model (PCNN)

In addition to the correlation model, a physics-constrained neural network (PCNN) approximation was constructed. Rather than employing a purely data-driven architecture, the network was designed to also embed essential physical constraints directly into its structure.

Note that physics-informed and physics-constrained neural-network approaches incorporate prior physical knowledge through the loss function, model architecture, or constrained output parametrization [34–36]. In this work, the present model follows a physics-constrained strategy by embedding selected physical properties directly into its model formulation and output parametrization, as described in the following.

6.2.1. Physical requirements

The neural network is set up such that Nu satisfies the following physical requirements:

1. Positivity: $\mathrm{Nu} > 0$.
2. Correct zero–Péclet limit: $\lim_{\mathrm{Pe}\to 0}\mathrm{Nu}(\lambda_1, \lambda_2, s_1, s_2, \mathrm{Pe}) = \mathrm{Nu}_0(\lambda_1, \lambda_2, s_1, s_2)$.
3. Non-negative enhancement: Increasing Pe should not decrease heat transfer.

To enforce these constraints, the network output was not modeled directly as Nu, but instead constructed in multiplicative form.

6.2.2. Network architecture

The input vector consists of five variables, $\boldsymbol{\xi} = [\lambda_1, \lambda_2, s_1, s_2]$ and Pe. The model is expressed as

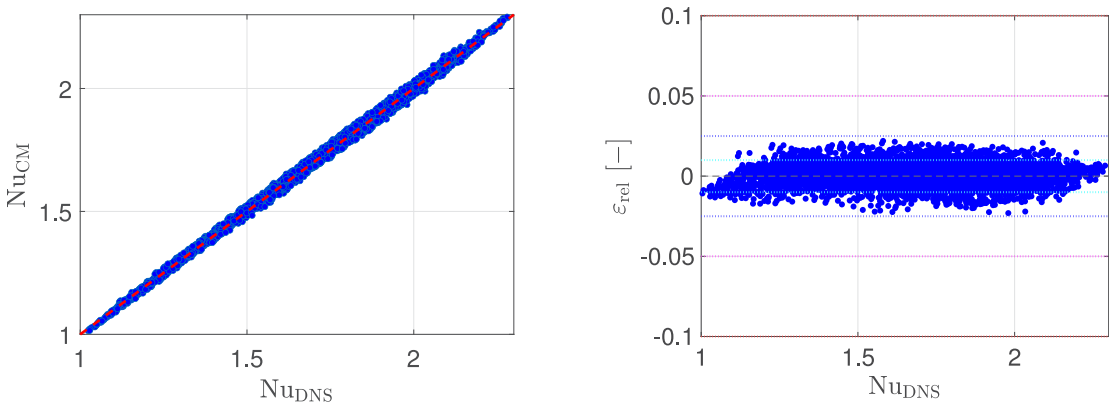
$$\mathrm{Nu}(\boldsymbol{x}) = \mathrm{Nu}_0(\boldsymbol{\xi})\left[1 + \mathrm{Pe}\, F(\boldsymbol{\xi}, \mathrm{Pe})\right], \tag{31}$$

where $\mathrm{Nu}_0(\boldsymbol{\xi})$ represents the baseline heat transfer at $\mathrm{Pe} = 0$, and $\mathrm{Pe}\, F(\boldsymbol{\xi}, \mathrm{Pe})$ represents the Pe-dependent enhancement factor. Observe that we again employ a multiplicative formulation, allowing the network to learn the diffusion-dominated contribution $\mathrm{Nu}_0(\boldsymbol{\xi})$ as a separate part. This enables a reduced representation for low Péclet number regimes ($\mathrm{Pe} \le 0.01$), where convection plays a negligible role, effectively providing again a standalone model for regimes where convective effects are negligible. To realize this structure, the neural network consists of two separate fully connected subnetworks:

Baseline branch (Nu_0). The baseline branch depends only on the shape parameters in $\boldsymbol{\xi}$ and has the following architecture: 4 input neurons, 3 hidden layers with 6, 6, and 4 neurons with tanh activation functions, output neuron with SoftPlus activation function ($\mathrm{Softplus}(z) = \ln(1 + e^z)$). The Softplus activation ensures $\mathrm{Nu}_0 > 0$.

Enhancement branch (F). The enhancement branch depends on the full input vector $(\boldsymbol{\xi}, \mathrm{Pe})$ and has the same depth and width as the baseline branch, i.e., 5 input neurons, three hidden layers with 6x6x4 neurons and tanh activation function and an output layer consisting of 1 neuron and a softplus activation function. The SoftPlus activation guarantees $F \ge 0$.

The hidden-layer architecture was selected based on the comparative architecture study reported in Appendix F. Five compact architectures were trained using identical data partitions, optimization settings, stopping criteria, and ten independent random initializations. Among the configurations considered, the $(6, 6, 4)$ architecture provided the lowest mean test-set NMSE, the highest mean test-set R^2, and the lowest mean maximum relative error. It was therefore selected as



(a) Predicted vs. DNS Nu number (b) Relative Error Distribution

Fig. 8. Analysis of the predictive accuracy of the Nusselt number correlation model.

the best compromise between compactness, predictive accuracy, and robustness.

6.2.3. Enforced physical constraints

With this architecture, several physical constraints are guaranteed by construction:

1. Since $\mathrm{Nu}_0 > 0$ and $F \geq 0$, we have $\mathrm{Nu} > 0$.
2. From Eq. (31), $\mathrm{Nu}(\mathrm{Pe} = 0) = \mathrm{Nu}_0$, so the zero Péclet limit is satisfied exactly.
3. For $\mathrm{Pe} \geq 0$, $\mathrm{Nu} \geq \mathrm{Nu}_0$, implying non-negative enhancement.

Thus, the multiplicative structure embeds essential physics into the model without reducing its expressive capability. To summarize, compared to a purely data-driven neural network, the present architecture: strictly enforces positivity, satisfies the correct asymptotic behavior for $\mathrm{Pe} \to 0$, guarantees non-negative enhancement, and improves stability outside the training range. The model therefore represents a hybrid between a physics-based surrogate formulation and a flexible nonlinear approximation.

As discussed in Section 6.1.3, the exact spherical limit $\mathrm{Nu} = 2$ as $\mathrm{Pe} \to 0$ is not imposed independently. The PCNN instead uses the DNS-based baseline Nu_0 together with the enforced non-negative convective enhancement, thereby remaining consistent with the sampled DNS database while preserving the prescribed zero-Péclet structure.

6.2.4. Loss function and training procedure

The dataset was split into a fixed test set (10% of the data) and a training pool. From the training pool, training and validation subsets were sampled for repeated experiments. Optimization was performed using the AdamW algorithm [32,33] with learning-rate scheduling, and early stopping was applied based on validation NMSE. The final model was selected according to the lowest test NMSE.

For the spherical configuration, the low-Pe behavior is additionally assessed against the Acrivos-Taylor asymptotic solution [31] as discussed in Section 6.1.3 and Appendix B.1.2.

6.2.5. Results: Physics-constrained neural network model

To assess robustness, $K = 10$ repeated training runs were performed using different random initializations. The best model, selected based on minimum test NMSE, achieved: $\mathrm{NMSE}_{\mathrm{best}} = 5.96 \times 10^{-6}$, $\mathrm{NMSE}_{\mathrm{mean}} = [1.00 \pm 0.39] \times 10^{-5}$ and $R^2_{\mathrm{test}} = 0.999533 \pm 0.000147$. These results demonstrate that the physics-constrained neural network provides highly accurate predictions across the complete parameter space.

Fig. 9(a) shows the predicted Nusselt number plotted against the corresponding measured values for the full dataset. The data points collapse tightly along the identity line ($\mathrm{Nu}_{\mathrm{NN}} = \mathrm{Nu}_{\mathrm{DNS}}$), confirming the absence of systematic bias. The extremely small scatter around the diagonal reflects the very high coefficient of determination ($R^2 \approx 0.9995$).

Furthermore, Fig. 9(b) displays the relative error $\varepsilon_{\mathrm{rel}}$ as a function of the measured Nusselt number. As observed, the vast majority of data points lie well within the $\pm 1\%$ bounds. The absence of structured error patterns indicates that the network captures the underlying physical trends consistently across the entire parameter range. The maximum observed deviation remains below 1.2%, demonstrating that the imposed physical constraints do not reduce predictive flexibility but instead stabilize and regularize the regression problem. The trained neural network is available on Zenodo [30].

6.3. Quantitative comparison between the correlation and the physics-constrained neural network model

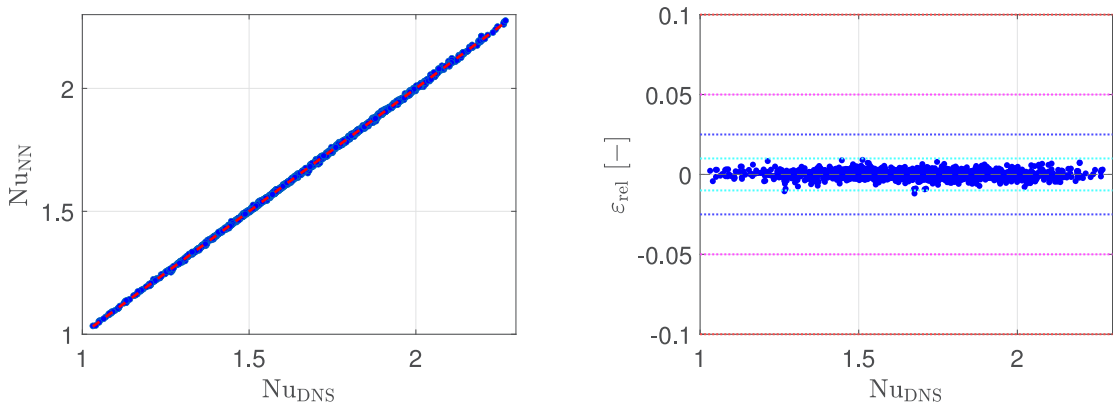
Both models achieve very high predictive accuracy. The correlation model provides a compact, physically interpretable representation with a limited number of basis functions.

For a consistent direct comparison, both models are evaluated here on the complete DNS dataset. The resulting metrics therefore compare their full-dataset interpolation accuracy. They should not be interpreted as a comparison of independent generalization performance, since only the PCNN was additionally evaluated on a held-out test set. On the full dataset, the physics-constrained neural network reaches $R^2_{\mathrm{full}} = 0.999735$, $\mathrm{mean}|\varepsilon_{\mathrm{rel}}| = 0.182\%$. The Nusselt number correlation model achieves comparable accuracy ($R^2_{\mathrm{full}} = 0.9982$) but with a slightly larger mean deviation ($\mathrm{mean}|\varepsilon_{\mathrm{rel}}| = 0.468\%$) and maximum deviation ($\max|\varepsilon_{\mathrm{rel}}| = 2.45\%$). Thus, on the full dataset, the PCNN exhibits slightly lower interpolation errors than the correlation model.

Model complexity comparison

A comparison of model complexity further highlights the structural differences between the correlation and the physics-constrained neural network model.

Correlation model. The correlation model employs: 25 basis functions for Φ^0, 6 basis functions for Φ^{η_1}, 10 basis functions for Φ^{η_2} and two global exponents (m and n). This results in 25 (Nu_0 coeff.) + 16 (enhancement coeff.) + 2 (exponents) = 43 trainable parameters in total. The resulting expression remains fully explicit and compact, with a closed-form evaluation cost proportional to the number of retained polynomial terms.



(a) Predicted vs. DNS Nu number (b) Relative Error Distribution

Fig. 9. Analysis of physics-constrained neural network predictive accuracy.

Physics-constrained neural network model. The PCNN consists of two subnetworks with the same hidden-layer architecture but different numbers of input variables. Each subnetwork contains three hidden layers with 6, 6, and 4 neurons and one output neuron. The baseline subnetwork receives the four shape parameters $(\lambda_1, \lambda_2, s_1, s_2)$ and therefore contains

$$[4\times 6+6]+[6\times 6+6]+[6\times 4+4]+[4\times 1+1]=105$$

trainable parameters. The enhancement subnetwork additionally receives the Péclet number and contains

$$[5\times 6+6]+[6\times 6+6]+[6\times 4+4]+[4\times 1+1]=111$$

trainable parameters. Consequently, the complete PCNN comprises $105 + 111 = 216$ trainable parameters. It therefore contains approximately 5.1 times more parameters than the analytical surrogate.

Computational cost comparison

Next, we compare the forward-evaluation cost of the two surrogate models. The Nusselt number correlation is evaluated using explicit polynomial and exponential operations, whereas the PCNN requires two feed-forward passes through small fully connected subnetworks. The (off-line) training cost is excluded from this comparison. This distinction is important because PCNN training involves gradient-based optimization and, in the physics-constrained setting, automatic differentiation of residual terms, making its (off-line) training cost substantially larger than the cost of fitting or evaluating the explicit correlation. Once trained, however, both models are inexpensive to evaluate, and the relevant quantity for deployment is the inference time per sample.

Since the surrogate models are intended to be evaluated locally for each tracked particle during a simulation time step, the relevant cost metric is the sequential single-sample inference time. Under this usage pattern, the Nusselt number correlation model required 1.42×10^{-5} s per evaluation, whereas the PCNN required 1.43×10^{-4} s per evaluation. Thus, the PCNN inference cost is approximately one order of magnitude larger than that of the correlation model. This suggests that, when embedded in a particle-tracking loop, the Nusselt number correlation is computationally preferable. Nevertheless, both models remain computationally inexpensive in absolute terms, with evaluation times on the order of 10^{-5}–10^{-4} s per call.

Discussion. Although the PCNN is computationally more expensive in the pointwise inference setting, both models remain compact, and their evaluation costs are small compared with many other operations typically performed in a coupled CFD-particle simulation. The correlation model offers higher interpretability and faster evaluation, whereas the PCNN provides greater representational flexibility and achieves improved accuracy. Notably, both approaches enforce the same physical constraints and asymptotic structure, illustrating that embedding physics into the model formulation, whether correlation-based or data-driven, leads to robust, efficient, and physically consistent representations compared with generic black-box architectures.

7. Summary and conclusions

In this work, we investigated convective heat transfer between non-spherical particles of superellipsoidal shape and a surrounding fluid in the Stokes-flow regime, with a particular focus on the influence of particle shape, its orientation and the flow condition. Superellipsoids provide a unified and flexible geometric representation that includes smooth ellipsoidal, cube-like, diamond-like, elongated, and plate-like particles within a continuous four-parameter shape space. This description is substantially richer than a purely ellipsoidal model, while remaining sufficiently compact for systematic DNS sampling and implementation in Lagrangian point-particle formulations.

Direct numerical simulations were performed over a broad parameter space defined by particle aspect ratios, shape exponents, orientations, and Péclet numbers. The orientational dependence of heat transfer was analyzed using the coefficient of variation of the Nusselt number across multiple flow configurations. We find that for $\mathrm{Pe} \leq 1$, orientation effects remain negligible over the investigated shape space, although convective enhancement becomes increasingly relevant for $0.001 \leq \mathrm{Pe} \leq 1$. In contrast, for $\mathrm{Pe} > 1$, convective effects lead to an increasing sensitivity to particle orientation. The magnitude of the orientation dependence is strongly shape-dependent: the investigated cube-like particles exhibit the smallest coefficient of variation, whereas diamond-like particles exhibit the largest.

Nevertheless, even at $\mathrm{Pe} \leq 1$, the numerical results demonstrate that particle shape has a significant impact on heat transfer characteristics. For all investigated shapes, the Nusselt number decreases with increasing particle aspect ratios, while deviations from ellipsoidal shapes $(s_1, s_2 \neq 1)$ introduce additional, independent variations that cannot be captured by aspect ratio alone. In particular, cubical particles consistently exhibit higher Nusselt numbers than more diamond-like variants for identical aspect ratio and flow conditions, highlighting the importance of local surface curvature and face orientation in determining heat transfer efficiency. Furthermore, we observed that for $\mathrm{Pe} \leq 0.01$ the Nusselt number depends only on shape and not on the Péclet number.

To enable efficient use of these findings in large-scale simulations, a Nusselt number correlation model and a PCNN model were developed

and compared to predict the Nusselt number as a function of particle shape and Péclet number.

The resulting surrogate models are valid within the investigated shape domain and for $\mathrm{Pe} \leq 1$. This Peclet-number restriction reflects the range used for training and validation and the intended application within a Stokes-regime point-particle framework; it should not be interpreted as a universal consequence of particle size or of the condition $\mathrm{Re}_\mathrm{p} \ll 1$.

Both models demonstrate excellent predictive accuracy across the investigated parameter space and provide computationally efficient alternatives to resolving particle-scale heat transfer in fully resolved simulations. The surrogate models are particularly well-suited for Lagrangian point-particle frameworks, where, at the carrier-flow-scale, particles may be treated as point entities while still accounting for shape-dependent thermal interactions with the fluid. Overall, the Nusselt number correlation model provides the most computationally efficient surrogate, being approximately 10× faster than the PCNN in pointwise inference. However, both models are sufficiently fast for repeated evaluations in coupled CFD-particle simulations ($10^{-5} - 10^{-4}$ s per evaluation). The PCNN achieves the highest accuracy, with errors below approximately 1%, while the correlation model remains highly accurate, with errors below approximately 2.5%. This highlights a clear trade-off: the correlation model offers superior speed and interpretability, whereas the PCNN provides improved accuracy and greater flexibility. The preferred choice therefore depends on the application requirements, particularly the relative importance of computational efficiency, interpretability, and predictive accuracy.

The applicability of the present results is subject to several important assumptions. The particle-scale flow is assumed to be in the asymptotic creeping-flow regime, $\mathrm{Re}_\mathrm{p} \ll 1$, so that fluid inertia is neglected and the surrounding velocity field is governed by the Stokes equations. The models' trained and validated thermal-transport range is $0.001 \leq \mathrm{Pe} \leq 1$. Since $\mathrm{Pe} = \mathrm{Re}_\mathrm{p}\,\mathrm{Pr}$, no independent universal range of Pr can be assigned: for a given fluid, the applicability must be assessed from the combined requirement $\mathrm{Re}_\mathrm{p} \ll 1$ and $\mathrm{Re}_\mathrm{p}\,\mathrm{Pr} \leq 1$. The models are therefore most directly relevant to fluids with Prandtl numbers of order unity or moderate magnitude under sufficiently small particle Reynolds numbers. In addition, the analysis assumes forced convection with negligible buoyancy, $\mathrm{Ri} \ll 1$, constant fluid properties, and an isothermal particle surface; application within a lumped point-particle energy balance further requires a sufficiently small particle Biot number.

Within these assumptions, the present study highlights that accurate prediction of particle–fluid heat transfer requires explicit consideration of particle shape beyond simple spherical or ellipsoidal approximations. The proposed modeling framework and surrogate approaches provide a robust and physically consistent basis for incorporating heat transfer effects of superellipsoidal particles in Stokes-regime applications such as aerosol transport, dilute particulate flows, and respiratory exposure modeling.

Supplementary data

The trained neural network has been deposited on Zenodo and is publicly available at [30].

CRediT authorship contribution statement

Jana Wedel: Writing – original draft, Visualization, Validation, Software, Methodology, Investigation, Formal analysis, Data curation, Conceptualization. **Ivan Dominik Horvat:** Writing – review & editing, Methodology, Investigation, Formal analysis, Conceptualization. **Matjaž Hriberšek:** Writing – review & editing, Supervision, Resources, Methodology, Investigation, Formal analysis, Conceptualization. **Paul Steinmann:** Writing – review & editing, Supervision, Resources, Project administration, Methodology, Funding acquisition, Formal analysis, Conceptualization. **Jure Ravnik:** Writing – review & editing, Supervision, Resources, Methodology, Investigation, Formal analysis, Conceptualization.

Declaration of competing interest

The authors declare that they have no known competing financial interests or personal relationships that could have appeared to influence the work reported in this paper.

Acknowledgments

The authors thank the Deutsche Forschungsgemeinschaft for the financial support in the framework of the project STE 544/75 and the Slovenian Research and Innovation Agency (research core funding No. P2-0196 and project J7-60118).

Appendix A. Particle-energy balance and lumped-capacitance formulation

A.1. General setting for particle-heat transfer

Here, we recall the general thermal balance for a solid particle. Although an isothermal particle with prescribed temperature is used in this work to determine the Nusselt number, the general formulation establishes the relation between internal heat conduction, the particle-averaged temperature, and the interfacial heat flux. In the solid particle, a rigid heat conductor, the temperature field $T_\mathrm{s} = T_\mathrm{s}(\boldsymbol{x}, t)$ is in general governed by a temperature evolution equation of diffusion type

$$\rho^\mathrm{s} c_\mathrm{p}^\mathrm{s} \frac{\partial T_\mathrm{s}}{\partial t} = -\nabla \cdot \boldsymbol{q}^\mathrm{s} \quad \text{with} \quad \boldsymbol{q}^\mathrm{s} = -k^\mathrm{s} \nabla T_\mathrm{s}\,, \tag{A.1}$$

where the heat flux in the particle is expressed by Fourier's law. Volume averaging the temperature evolution equation for the particle and using the Gauss divergence theorem on the right-hand side results in

$$\rho^\mathrm{s} c_\mathrm{p}^\mathrm{s} \frac{\partial \langle T_\mathrm{s} \rangle}{\partial t} = -\frac{A}{V} \langle q_\mathrm{n} \rangle_\Gamma \quad \text{with} \quad q_\mathrm{n} := \boldsymbol{q}^\mathrm{s} \cdot \boldsymbol{n} \quad \text{and} \quad \langle \{\bullet\} \rangle := \frac{1}{V} \int_V \{\bullet\}\, \mathrm{d}V$$
$$\text{and} \quad \langle \{\circ\} \rangle_\Gamma := \frac{1}{A} \int_\Gamma \{\circ\}\, \mathrm{d}A\,, \tag{A.2}$$

where q_n is the scalar-valued (normal) heat flux from the particle to the fluid and V and A denote the volume and the surface area of the particle, respectively. Note that $d_\mathrm{eq} \propto V/A$.

A.2. Lumped-capacitance model for the particle

Within the particle, the relative importance of internal heat conduction and convective heat transfer through Γ is quantified by the Biot number

$$\mathrm{Bi} := \frac{h\, d_\mathrm{eq}}{k^s}\,. \tag{A.3}$$

For $\mathrm{Bi} \ll 1$, heat conduction within the particle is sufficiently fast to justify the assumption of a spatially uniform temperature field; thus $T_\mathrm{s} = T_\mathrm{s}(t)$. In this scenario, the particle satisfies the assumption of the lumped-capacitance model, in which the particle temperature is spatially uniform, thus $\Delta T \equiv \langle \Delta T \rangle_\Gamma$, but varies in time with $T_\mathrm{s} = T_\mathrm{s}(t)$. Importantly, this assumption does not imply that the particle and the fluid temperature coincide instantaneously. This is obvious when the lumped-capacitance assumption and the convective interface condition of Robin-type are incorporated into the spatially averaged temperature evolution equation for the particle. This results in an evolution equation for the relative temperature with exponentially decaying solution

$$\frac{\mathrm{d}\Delta T}{\mathrm{d}t} = -\frac{\Delta T}{\tau^\mathrm{s}} \quad \rightsquigarrow \quad \Delta T(t) = \Delta T(0)\, e^{-t/\tau^\mathrm{s}} \tag{A.4}$$

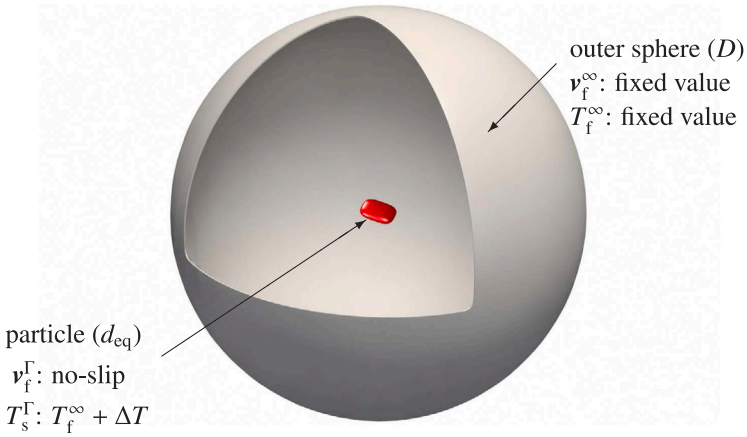


Fig. B.1. Visualization of problem setup: The solution domain is bounded by an outer sphere of diameter D and a particle of volume-equivalent size d_eq positioned at the center of the outer sphere. Furthermore, the employed boundary conditions are denoted. Note that $d_\mathrm{eq} \ll D$. The ratio of the outer domain diameter D to the equivalent particle diameter d_eq is $D/d_\mathrm{eq} = 1024$. The displayed particle is scaled by a factor of 50 for visualization purposes. The particle velocity is set to $\boldsymbol{v}_\mathrm{s} = \boldsymbol{0}$, thus here the relative velocity is $\boldsymbol{u} \equiv \boldsymbol{v}_\mathrm{f}^{\infty}$.

$$\text{with} \quad \tau^\mathrm{s} := \rho^\mathrm{s} c_\mathrm{p}^\mathrm{s} \frac{V}{A} \frac{1}{h} \propto \rho^\mathrm{s} c_\mathrm{p}^\mathrm{s} \frac{d_\mathrm{eq}}{h} = \frac{\rho^\mathrm{s} c_\mathrm{p}^\mathrm{s}}{k^\mathrm{f}} \frac{d_\mathrm{eq}^2}{\mathrm{Nu}}, \tag{A.5}$$

where τ^s denotes the characteristic time for the particle to adapt to the fluid temperature. When τ^s is small compared with the characteristic timescale of the surrounding flow, the particle adopts the ambient fluid temperature instantaneously, for larger τ^s the particle temperature lags behind the ambient fluid temperature.

Appendix B. Mesh sensitivity study

The fluid domain was discretized using a predominantly hexahedral, locally split-hexahedral/polyhedral finite-volume mesh generated with the OpenFOAM snappyHexMesh utility. Local refinement was applied near the particle surface to resolve the velocity and temperature gradients.

The mesh was generated in three steps. First, a uniform Cartesian background mesh was created with blockMesh over a cubic domain extending from −700 to 700 in each coordinate direction, using 25^3 hexahedral cells. In the first snappyHexMesh stage, the domain was reduced to the spherical computational region and progressively refined toward the particle location using concentric spherical refinement regions with radii $150, 40, 20, 8, 6, 4$, and 2, corresponding to refinement levels $2, 3, 4, 5, 6, 8$, and 9, respectively. In the second snappyHexMesh stage, the mesh was snapped to the actual particle surface, which was refined to level 11; additional distance-based refinement was applied in its immediate vicinity, and three surface-normal cell layers were added.

The outer-domain diameter was chosen such that $D/d_\mathrm{eq} = 1024$. This choice follows the computational-domain sizing analysis performed in our previous study of Stokes flow around superellipsoidal particles, in which an outer-domain size of $1024 d_\mathrm{eq}$ was found to provide an adequate approximation of the unbounded-flow condition [27]. A mesh sensitivity analysis is performed to determine the level of discretization required to accurately resolve the flow around the superellipsoidal particles in the Stokes regime. This analysis constitutes a prerequisite for the subsequent evaluation of the Nusselt number. A visualization of the problem setup along with the boundary conditions is provided in Fig. B.1. Both spherical and non-spherical particles are considered, which are suspended in a local flow field with the relative fluid velocity $\boldsymbol{u}$ prescribed exclusively along the major axis of the particle; the coefficients of $\boldsymbol{u}$ read in the particle frame of reference as $\underline{u}' = [1, 0, 0]$. Note that the simulations are performed using a custom solver developed in OpenFOAM V11 [22] to solve the Stokes-flow equations.

B.1. Spherical particle

B.1.1. Drag-force convergence and analytical validation

Before examining the mesh sensitivity for non-spherical particles, it is useful to recall reference values obtained from analytical solutions for spherical particles. In particular, for a spherical particle suspended in Stokes flow, the magnitude of the drag force is given by $F_\mathrm{sph,Stk} = 3\,\pi\,\mu^\mathrm{f}\,d_\mathrm{eq}\,U$. Thus, in the following, we analyze the dimensionless drag force defined as $F^* := F_\mathrm{d}/F_\mathrm{sph,Stk}$, where F_d denotes the drag force for a generic particle shape. For a spherical particle under Stokes-flow conditions, this yields $F^* = 1$ and serves as a reference to assess the numerical accuracy of the Stokes flow calculations. The details of the mesh sensitivity study for spherical particles are summarized in Table B.3.

Note that t_mesh denotes the wall-clock time required for mesh generation, whereas t_sim denotes the wall-clock time required for the numerical simulation. All runtimes were measured in serial on the same workstation and using identical computational settings.

Obviously, the differences in the computed drag force magnitude decrease with increasing mesh refinement. Moreover, finer meshes yield smaller deviations from the analytical Stokes drag reference. In general, the deviations remain low for all meshes considered; even the coarsest mesh (M0) exhibits a relative deviation of only −0.6% from the analytical solution.

B.1.2. Thermal mesh convergence at low péclet number

Furthermore, it is well known that for a spherical particle in the limit of vanishing Péclet number ($\mathrm{Pe} \to 0$), heat transfer is purely diffusive and governed by stagnant conduction, yielding the classical result $\mathrm{Nu} = 2$. Therefore, this analytical value serves as a reference for validating the numerical accuracy of the OpenFOAM heat transfer solver in the low Pe regime.

The mesh sensitivity study summarized in Table B.4 demonstrates systematic convergence of the Nusselt number toward the analytical limit with increasing mesh resolution. In particular, for mesh ID M2, the relative deviation from the reference value is below 0.6%. Consequently, mesh M2 is adopted for all subsequent simulations, as it ensures adequate accuracy in both fluid flow and heat transfer simulations at a substantially lower computational cost than mesh M3.

Fig. B.2 illustrates the variation of the Nusselt number with the Péclet number for a spherical particle in the Stokes flow regime using mesh M2. As expected, Nu increases monotonically with increasing Pe, reflecting the growing contribution of convective heat transfer. In the limit $\mathrm{Pe} \to 0$, the numerical results recover the analytical value

Table B.3
Mesh sensitivity study for a spherical particle (drag forces): $\lambda_1 = \lambda_2 = 1$; $s_1 = s_2 = 1$. Note that $F_{\mathrm{sph,Stk}} = \left[3\pi\mu^{\mathrm{f}} d_{\mathrm{eq}} U\right]$ and $\epsilon_{\mathrm{sph,Stk}} = \left[F^* - F_{\mathrm{Stk}}\right]/F_{\mathrm{Stk}}$. The runtime comparison was conducted serially on a local workstation running Ubuntu 24.04.4 LTS and equipped with an Intel Xeon E5-2650 v3 processor operating at 2.30 GHz. All mesh configurations were tested using a single process and otherwise identical computational settings.

Visualization (M2)		Mesh ID	Particle surface elements	Overall cells	t_{mesh} [s]	t_{sim} [s]	Force F^* [−] $F_{\mathrm{d}}/F_{\mathrm{sph,Stk}}$	$\epsilon_{\mathrm{sph,Stk}}$ [%] [%]
	Sphere	M0	992	1888	11	225	0.9940	−0.603%
		M1	1512	30 856	17	395	0.9949	−0.513%
		M2	2336	51 440	29	684	0.9972	−0.282%
		M3	3624	92 780	48	1286	0.9985	−0.153%

Table B.4
Mesh sensitivity study for a spherical particle (Nu) with Pe = 0.001: $\lambda_1 = \lambda_2 = 1$; $s_1 = s_2 = 1$.

	M0	M1	M2	M3
Nu [−]	1.98129	1.9836	1.9884	1.99539
$\epsilon^{\mathrm{Nu}}_{\mathrm{Pe}\to 0}$ [%]	−0.936%	−0.820%	−0.580%	−0.231%

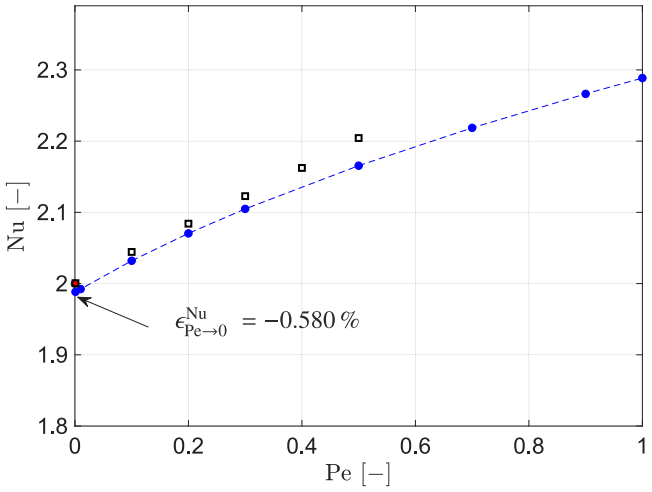


Fig. B.2. Dependence of Nu on Pe for a spherical particle in Stokes flow. Selected Mesh ID: M2. ● present model results, □ Acrivos and Taylor [31], ● reference result Nu = 2 for Pe → 0. Note that the low-Pe asymptotic solution of Acrivos and Taylor [31] is shown up to Pe = 0.5.

with sufficient precision. In summary, we confirm the accuracy of the selected mesh for resolving coupled flow and heat transfer effects for spherical particles.

The low-Péclet-number asymptotic solution of Acrivos and Taylor [31] is additionally shown in Fig. B.2. Note that their expansion is formulated in terms of the radius-based Péclet number Pe^*. Thus, the present diameter-based definition corresponds to $\mathrm{Pe}^* = \mathrm{Pe}/2$. The theoretical solution is shown up to Pe = 0.5 ($\mathrm{Pe}^* = 0.25$). Very close agreement with the DNS is observed in the asymptotic low-Pe regime, particularly for $\mathrm{Pe} \lesssim 0.3$ (deviations below −0.8432%), while the deviation gradually increases as Pe increases, as expected for a small-Pe asymptotic expansion

B.2. Ellipsoidal particles

The numerical accuracy for non-spherical particles is first assessed for two representative ellipsoids: a prolate spheroid characterized by $(\lambda_1, \lambda_2, s_1, s_2) = (5, 1, 1, 1)$ and an oblate spheroid characterized by $(\lambda_1, \lambda_2, s_1, s_2) = (5, 5, 1, 1)$. For both geometries, the imposed relative velocity is aligned with the x_1-axis, i.e. $\boldsymbol{u} = [u_x, 0, 0]$. Consequently, the flow is parallel to the symmetry axis of the prolate spheroid and perpendicular to the symmetry axis of the oblate spheroid. Four successively refined meshes, denoted by M0–M3, are considered.

B.2.1. Drag-force convergence and analytical validation

The numerical drag forces for the ellipsoidal particles are compared with the analytical creeping-flow resistance expressions reported by Happel and Brenner [37]. For an axisymmetric spheroid, the hydrodynamic force can be expressed as

$$\boldsymbol{F}_{\mathrm{d}} = \zeta_{\parallel}\boldsymbol{U}_{\parallel} + \zeta_{\perp}\boldsymbol{U}_{\perp}, \tag{B.1}$$

where $\zeta_{\parallel}$ and $\zeta_{\perp}$ denote the translational resistance coefficients for motion parallel and perpendicular to the spheroid symmetry axis, respectively.

For a prolate spheroid with major semi-axis a_1 and equal minor semi-axes $a_2 = a_3$, the eccentricity is

$$e_{\mathrm{pro}} = \sqrt{1 - a_2^2/a_1^2}. \tag{B.2}$$

The resistance coefficient for translation parallel to the major axis is

$$\zeta_{\parallel}^{\mathrm{pro}} = 6\pi\mu^{\mathrm{f}} a_1 \frac{\frac{8}{3}e_{\mathrm{pro}}^3}{-2e_{\mathrm{pro}} + \left[1 + e_{\mathrm{pro}}^2\right]\ln\left(\frac{1+e_{\mathrm{pro}}}{1-e_{\mathrm{pro}}}\right)}. \tag{B.3}$$

For an oblate spheroid with equal equatorial semi-axes $a_1 = a_2 > a_3$, the eccentricity is

$$e_{\mathrm{obl}} = \sqrt{1 - a_3^2/a_1^2}. \tag{B.4}$$

Because the imposed flow is aligned with a_1, it is perpendicular to the oblate symmetry axis a_3. The corresponding resistance coefficient is

$$\zeta_{\perp}^{\mathrm{obl}} = 6\pi\mu^{\mathrm{f}} a_1 \frac{\frac{8}{3}e_{\mathrm{obl}}^3}{\left[1 + 2e_{\mathrm{obl}}^2\right]\sin^{-1}\left(e_{\mathrm{obl}}\right) - e_{\mathrm{obl}}\sqrt{1 - e_{\mathrm{obl}}^2}}. \tag{B.5}$$

The analytical drag force is obtained from

$$F_{\mathrm{d,HB}} = \zeta U. \tag{B.6}$$

Both the numerical and analytical drag forces are normalized by the Stokes drag of a volume-equivalent sphere,

$$F_{\mathrm{sph,Stk}} = 3\pi\mu^{\mathrm{f}} d_{\mathrm{eq}} U, \tag{B.7}$$

such that

$$F_{\mathrm{d}}^* = \frac{F_{\mathrm{d}}}{F_{\mathrm{sph,Stk}}}, \qquad F_{\mathrm{d,HB}}^* = \frac{F_{\mathrm{d,HB}}}{F_{\mathrm{sph,Stk}}}. \tag{B.8}$$

The signed relative deviation from the analytical result is defined as

$$\epsilon_{\mathrm{HB}} = \frac{F_{\mathrm{d,DNS}}^* - F_{\mathrm{d,HB}}^*}{F_{\mathrm{d,HB}}^*}. \tag{B.9}$$

For the geometries considered here, Eqs. (B.3) and (B.5) give $F_{\mathrm{d,HB}}^* = 1.0438$ for the prolate spheroid and $F_{\mathrm{d,HB}}^* = 1.1279$ for the oblate spheroid. The numerical results and their deviations from the analytical values are summarized in Table B.5.

For the prolate spheroid, the deviation from the analytical Happel–Brenner result decreases from −1.175% on mesh M0 to −0.313% on mesh M3. The result obtained on the selected mesh M2 differs from the analytical value by only −0.571%.

For the oblate spheroid, all mesh levels agree with the analytical result to within approximately 0.64%, while the M2 result differs by

Table B.5
Mesh convergence and analytical validation of the dimensionless drag force for representative prolate and oblate spheroids. The numerical results are compared with the creeping-flow resistance expressions of Happel and Brenner [37], see Eq. (B.9). The analytical values are $F^*_{\mathrm{d,HB}} = 1.0438$ for the prolate spheroid and $F^*_{\mathrm{d,HB}} = 1.1279$ for the oblate spheroid. The runtime comparison was conducted serially on a local workstation running Ubuntu 24.04.4 LTS and equipped with an Intel Xeon E5-2650 v3 processor operating at 2.30 GHz. All mesh configurations were tested using a single process and otherwise identical computational settings.

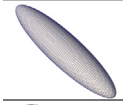
Visualization (M2)		Mesh ID	Particle-surface elements	Overall cells	t_{mesh} [s]	t_{sim} [s]	$F^*_{\mathrm{d,DNS}}$ $F_{\mathrm{d}}/F_{\mathrm{sph,Stk}}$	ϵ_{HB} [%]
	Prolate	M0	1488	23 104	12	238	1.0315	−1.175
		M1	2232	35 608	18	396	1.0347	−0.868
		M2	3424	60 560	34	923	1.0378	−0.571
		M3	5296	106 364	59	1943	1.0405	−0.313
	Oblate	M0	1808	23 644	15	274	1.1214	−0.574
		M1	2712	38 069	20	508	1.1207	−0.636
		M2	4192	63 931	35	951	1.1229	−0.441
		M3	6472	111 962	62	1896	1.1211	−0.601

Table B.6
Mesh-sensitivity study of the Nusselt number for the representative prolate and oblate spheroids at $\mathrm{Pe} = 0.001$ and $\boldsymbol{u} = [u_x, 0, 0]$. The relative changes are evaluated between successive mesh levels.

Particle	Quantity	M0	M1	M2	M3
Prolate	Nu	1.80851	1.81255	1.81672	1.82346
	$\epsilon^{\mathrm{Nu}}_{\mathrm{rel}}$ [%]	–	0.2234	0.2301	0.3710
Oblate	Nu	1.51829	1.51930	1.52159	1.52602
	$\epsilon^{\mathrm{Nu}}_{\mathrm{rel}}$ [%]	–	0.0665	0.1507	0.2911

−0.441%. The small non-monotonic variation with mesh refinement is of the same order as the remaining discretization and domain-truncation errors. Overall, the comparison confirms that the numerical Stokes-flow solution accurately reproduces the hydrodynamic resistance of both prolate and oblate spheroids.

B.2.2. Thermal mesh convergence at low Péclet number

Before comparing the numerical heat-transfer results with Brenner's low-Pe theory, the thermal mesh convergence is assessed at $\mathrm{Pe} = 0.001$. This value is used in the subsequent analytical comparison and lies in the diffusion-dominated regime in which Brenner's asymptotic result is applicable.

Table B.6 reports the Nusselt numbers and the signed relative changes between successive mesh levels.

For the prolate spheroid, the relative difference between meshes M2 and M3 is 0.371%, while the corresponding difference for the oblate spheroid is 0.291%. The Nusselt numbers obtained on M2 are therefore sufficiently converged for use in the following comparison with Brenner's analytical low-Pe result.

B.2.3. Validation against Brenner's low-Péclet-number result

Having established the thermal mesh convergence at $\mathrm{Pe} = 0.001$, the Nusselt numbers obtained on mesh M2 are compared with the analytical low-Pe result of Brenner [6].

Brenner derived the leading-order forced-convection correction to heat or mass transfer from an isothermal particle of arbitrary shape in an unbounded laminar flow. The analysis applies in the asymptotic limit $\mathrm{Pe} \ll 1$, in which the temperature field is treated as a perturbation of the stagnant-fluid pure-conduction solution. Accordingly, the Nusselt number may be expressed as

$$\mathrm{Nu} = \mathrm{Nu}_0 + \mathrm{Pe}\,\mathrm{Nu}_1 + o(\mathrm{Pe}), \tag{B.10}$$

where Nu_0 denotes the stagnant-fluid Nusselt number and Nu_1 represents the leading convective correction. The present validation employs this leading-order low-Pe expression. Higher-order terms in Brenner's formulation additionally involve the hydrodynamic resistance of the particle. The corresponding drag-force calculations are independently validated against analytical Happel–Brenner resistance expressions in B.2.1

For the definitions adopted in the present work, $\mathrm{Pe} = U d_{\mathrm{eq}}/\alpha^{\mathrm{f}}$, $\mathrm{Nu} = Q d_{\mathrm{eq}}/\left[A k^{\mathrm{f}} \Delta T\right]$, where A is the particle surface area and Q is the total heat transfer rate, Brenner's result can be written as

$$\mathrm{Nu}_{\mathrm{Brenner}} = \mathrm{Nu}_0 \left[1 + \frac{\mathrm{Pe}C}{2d_{\mathrm{eq}}}\right] + o(\mathrm{Pe}), \tag{B.11}$$

where C is a geometry-dependent shape coefficient with dimensions of length. The pure-conduction heat-transfer rate is related to C by

$$Q_0 = 4\pi k^{\mathrm{f}} C \Delta T. \tag{B.12}$$

Substitution into the definition of the Nusselt number gives

$$\mathrm{Nu}_0 = 4\pi C d_{\mathrm{eq}}/A\,. \tag{B.13}$$

Eq. (B.11) can therefore equivalently be expressed as

$$\mathrm{Nu}_{\mathrm{Brenner}} = \mathrm{Nu}_0 + \mathrm{Pe}\frac{\mathrm{Nu}_0^2\, A}{8\pi d_{\mathrm{eq}}^2} + o(\mathrm{Pe}). \tag{B.14}$$

Although Brenner's result is valid for particles of arbitrary shape, its quantitative evaluation requires the shape-dependent pure-conduction solution, or equivalently the shape coefficient C. For a general superellipsoid, this quantity is not available in closed form. The independent quantitative validation is therefore performed for the ellipsoidal subset ($s_1 = s_2 = 1$), for which C can be evaluated from the ellipsoid integral

$$C = 2\left[\int_0^\infty \mathrm{d}\xi \Big/ \sqrt{\left[a_1^2+\xi\right]\left[a_2^2+\xi\right]\left[a_3^2+\xi\right]}\right]^{-1}. \tag{B.15}$$

For axisymmetric spheroids, Eq. (B.15) can be evaluated analytically. For a prolate spheroid with $a_1 > a_2 = a_3$,

$$C = \frac{2a_1 e}{\ln\left(\frac{1+e}{1-e}\right)}, \qquad e = \sqrt{1 - \frac{a_2^2}{a_1^2}}, \tag{B.16}$$

whereas for an oblate spheroid with $a_1 = a_2 > a_3$,

$$C = \frac{a_1 e}{\sin^{-1}(e)}, \qquad e = \sqrt{1 - \frac{a_3^2}{a_1^2}}. \tag{B.17}$$

These analytical expressions are used for the axisymmetric spheroids, while Eq. (B.15) is evaluated numerically for the general triaxial ellipsoids. For the volume-preserving parametrization employed here, the semi-axes of an ellipsoid are $a_1 = \lambda_1 a_3$, $a_2 = \lambda_2 a_3$, $a_3 = d_{\mathrm{eq}}/\left[2[\lambda_1\lambda_2]^{1/3}\right]$. The surface area A is evaluated numerically for the general ellipsoidal geometry, while C is obtained analytically for axisymmetric spheroids and from Eq. (B.15) for the remaining triaxial ellipsoids. These quantities are then used to calculate Nu_0 from Eq. (B.13) and $\mathrm{Nu}_{\mathrm{Brenner}}$ from Eq. (B.14). Fig. B.3 compares the analytical predictions with the corresponding DNS values obtained on mesh M2 at $\mathrm{Pe} = 0.001$.

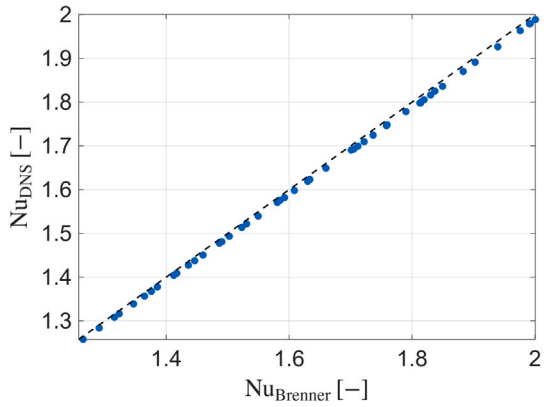


Fig. B.3. Comparison of the DNS Nusselt numbers obtained on mesh M2 at Pe = 0.001 with the low-Pe asymptotic prediction of Brenner [6] for all investigated ellipsoidal particles with $s_1 = s_2 = 1$ and $1 \le \lambda_2 \le \lambda_1 \le 9$. The dashed line denotes exact agreement.

Table B.7
Mesh-sensitivity study of the Nusselt number for the representative prolate and oblate spheroids at Pe = 1 and $\boldsymbol{u} = [u_x, 0, 0]$. The relative changes are evaluated between successive mesh levels.

Particle	Quantity	M0	M1	M2	M3
Prolate	Nu	2.12807	2.13253	2.13760	2.14096
	ϵ_{rel}^{Nu} [%]	–	0.2096	0.2377	0.1572
Oblate	Nu	1.78906	1.79004	1.79279	1.79442
	ϵ_{rel}^{Nu} [%]	–	0.0548	0.1536	0.0909

The relative deviation for ellipsoidal shape i is defined as

$$\epsilon_B^i = \left| \left[\mathrm{Nu}_{DNS}^i - \mathrm{Nu}_{Brenner}^i \right] / \mathrm{Nu}_{Brenner}^i \right|. \tag{B.18}$$

The spherical limit provides an additional consistency check. For a sphere, $C = d_{eq}/2$, $A = \pi d_{eq}^2$ and consequently $\mathrm{Nu}_0 = 2$. Thus, Eq. (B.11) recovers the corresponding low-Pe correction in the present normalization. The close agreement in Fig. B.3 confirms that the thermal solver reproduces both the shape-dependent pure-conduction contribution and Brenner's leading low-Pe behavior with sufficient accuracy. Over all ellipsoidal geometries considered, the mean and maximum relative deviations are 0.641% and 0.843%, respectively. These deviations are of the same order as the remaining numerical discretization error identified in the preceding mesh-convergence study.

B.2.4. Thermal mesh sensitivity at Pe = 1

The Brenner comparison is necessarily restricted to the asymptotic low-Pe regime and therefore does not assess numerical resolution at the upper end of the parameter range considered in this work. To address this point, the thermal mesh-sensitivity study is repeated at Pe = 1, which is the highest Péclet number included in the surrogate training and validation range. The corresponding results are summarized in Table B.7.

At Pe = 1, the relative difference between meshes M2 and M3 is 0.157% for the prolate spheroid and 0.091% for the oblate spheroid. Thus, the selected mesh M2 remains sufficiently resolved at the largest Péclet number considered in the surrogate-model range.

Taken together, the analytical drag-force comparison, the low-Pe Brenner validation, and the mesh-sensitivity studies at Pe = 0.001 and Pe = 1 demonstrate that mesh M2 provides an appropriate compromise between numerical accuracy and computational cost for the ellipsoidal cases considered in the DNS database.

B.3. Non-ellipsoidal superellipsoidal particles

The preceding subsection employs explicit analytical reference solutions that can be evaluated for ellipsoidal particles. Classical theoretical studies also provide general formulations for creeping flow and low-Péclet-number heat or mass transfer around particles of arbitrary shape. Such formulations may involve shape-dependent boundary-value problems, resistance tensors, or shape-dependent coefficients and do not necessarily yield simple explicit expressions for a prescribed particle geometry.

For the particular cube-like and diamond-like superellipsoids considered here, we are not aware of directly evaluable analytical expressions for either the hydrodynamic resistance or the shape-dependent pure-conduction contribution required in Brenner's low-Pe law. The numerical accuracy for these geometries is therefore assessed through systematic mesh-refinement studies.

Two representative non-ellipsoidal superellipsoids are considered. The first is a cube-like prolate particle $(\lambda_1, \lambda_2, s_1, s_2) = (5, 1, 0.2, 0.2)$ whereas the second is a diamond-like prolate particle $(\lambda_1, \lambda_2, s_1, s_2) = (5, 1, 1.8, 1.8)$. For both particles, the imposed relative velocity is aligned with the x_1-axis, $\boldsymbol{u} = [u_x, 0, 0]$. The same four successively refined meshes M0–M3 as in the preceding ellipsoidal study are considered.

B.3.1. Drag-force mesh convergence

For the non-ellipsoidal superellipsoids considered here, the hydrodynamic solution is assessed by examining the convergence of the dimensionless drag force between successive mesh levels. Table B.8 summarizes the mesh statistics, the normalized drag forces, and the corresponding relative changes between successive mesh levels.

For the cube-like particle, the magnitude of the relative change decreases from 0.33% between M0 and M1 to 0.10% between M2 and M3. For the diamond-like particle, the corresponding M2-to-M3 change is 0.263%. These results indicate that mesh M2 provides a sufficiently resolved hydrodynamic solution for the non-ellipsoidal superellipsoids considered here.

B.3.2. Nusselt-number mesh convergence

Brenner's low-Pe theory is applicable to isothermal particles of arbitrary shape. Its quantitative evaluation nevertheless requires the shape-dependent pure-conduction solution, which can equivalently be expressed in terms of the geometry-dependent shape coefficient C. For the ellipsoids considered in the preceding subsection, this quantity can be obtained from the analytical ellipsoid integral. For arbitrary superellipsoids, no comparably simple directly evaluable expression for this quantity is available. Consequently, we assess the thermal solution of the two considered superellipsoids through direct mesh refinement at Pe = 0.001 and Pe = 1.

Table B.9 summarizes the Nusselt numbers and the relative changes between successive mesh levels at Pe = 0.001. Observe that the relative difference between the M2 and M3 results is 0.258% for the cube-like particle and 0.240% for the diamond-like particle. The selected M2 mesh therefore provides an effectively mesh-independent prediction of the Nusselt number in the diffusion-dominated regime.

At Pe = 1, the relative difference between the M2 and M3 results is 0.038% for the cube-like particle and 0.008% for the diamond-like particle, see Table B.10. Thus, the selected M2 mesh remains sufficiently resolved at the largest Péclet number included in the surrogate-model range.

The convergence is not strictly monotonic for every particle and integral quantity. This behavior is expected because the meshes at the different refinement levels are generated independently and the Nusselt number is obtained from surface-normal temperature gradients, which are particularly sensitive to the local surface discretization. Nevertheless, the absolute M2-to-M3 differences remain below 0.3% for all drag-force and Nusselt-number results presented in this subsection.

Table B.8
Mesh-sensitivity study of the dimensionless drag force for representative non-ellipsoidal superellipsoids. The cube-like and diamond-like particles are characterized by $(\lambda_1, \lambda_2) = (5, 1)$ and by $s_1 = s_2 = 0.2$ and $s_1 = s_2 = 1.8$, respectively. The imposed relative velocity is $\boldsymbol{u} = [u_x, 0, 0]$. The runtime comparison was conducted serially on a local workstation running Ubuntu 24.04.4 LTS and equipped with an Intel Xeon E5-2650 v3 processor operating at 2.30 GHz. All mesh configurations were tested using a single process and otherwise identical computational settings.

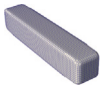
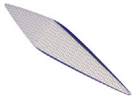
Visualization (M2)		Mesh ID	Particle-surface elements	Overall cells	t_{mesh} [s]	t_{sim} [s]	F_{d}^{*} $F_{\text{d}}/F_{\text{sph,Stk}}$	$\epsilon_{\text{rel}}^{F}$ [%]
	Cube-like	M0	1704	23 460	12	286	1.0743	–
		M1	2584	35 784	20	478	1.0782	0.33
		M2	4088	65 136	35	981	1.0770	−0.11
		M3	6208	111 996	57	1987	1.0759	−0.10
	Diamond-like	M0	1448	23 764	13	290	1.0918	–
		M1	2184	37 448	21	480	1.0981	0.578
		M2	3918	63 704	37	979	1.1022	0.365
		M3	5176	112 940	69	1968	1.1051	0.263

Table B.9
Mesh-sensitivity study of the Nusselt number for representative non-ellipsoidal superellipsoids at Pe = 0.001 and $\boldsymbol{u} = [u_x, 0, 0]$. The cube-like and diamond-like particles are characterized by $(\lambda_1, \lambda_2) = (5, 1)$ and by $s_1 = s_2 = 0.2$ and $s_1 = s_2 = 1.8$, respectively. The relative changes are evaluated between successive mesh levels.

Particle	Quantity	M0	M1	M2	M3
Cube-like	Nu	1.71746	1.71828	1.71385	1.71827
	$\epsilon_{\text{rel}}^{\text{Nu}}$ [%]	–	0.0477	−0.2578	0.2579
Diamond-like	Nu	1.72660	1.72911	1.73220	1.73636
	$\epsilon_{\text{rel}}^{\text{Nu}}$ [%]	–	0.1454	0.1787	0.2402

Table B.10
Mesh-sensitivity study of the Nusselt number for representative non-ellipsoidal superellipsoids at Pe = 1 and $\boldsymbol{u} = [u_x, 0, 0]$. The cube-like and diamond-like particles are characterized by $(\lambda_1, \lambda_2) = (5, 1)$ and by $s_1 = s_2 = 0.2$ and $s_1 = s_2 = 1.8$, respectively. The relative changes are evaluated between successive mesh levels.

Particle	Quantity	M0	M1	M2	M3
Cube-like	Nu	2.01966	2.02093	2.01547	2.01623
	$\epsilon_{\text{rel}}^{\text{Nu}}$ [%]	–	0.0629	−0.2702	0.0377
Diamond-like	Nu	2.04651	2.04990	2.05423	2.05439
	$\epsilon_{\text{rel}}^{\text{Nu}}$ [%]	–	0.1656	0.2112	0.0078

Taken together, the drag-force and thermal mesh-refinement studies show that mesh M2 provides an appropriate compromise between numerical accuracy and computational cost for the non-ellipsoidal superellipsoids employed in the DNS database.

Appendix C. Shape dependence of the thermal power exchange

While the Nusselt number characterizes the normalized heat-transfer coefficient, it does not directly quantify the total amount of heat transferred by the particle. In the present study, the particle volume, and therefore the volume-equivalent diameter d_{eq}, is kept constant, whereas the particle surface area A varies with shape. Consequently, a particle with a comparatively lower Nusselt number may still transfer more heat if its larger surface area compensates for, or outweighs, the reduction in the heat-transfer coefficient.

The resultant total heat flux, that is, the thermal power exchange Q $[W]$ between a particle and the surrounding fluid is related to the Nusselt number as follows

$$Q := \int_{\Gamma} q_{\text{n}} \,\mathrm{d}A = A \,\langle q_{\text{n}} \rangle_{\Gamma} = A\, h\, \Delta T = \text{Nu}\, k^{\text{f}}\, \frac{A}{d_{\text{eq}}}\, \Delta T\,. \tag{C.1}$$

As a reference, for a sphere at Pe $\to$ 0 the Nusselt number is $\text{Nu}_{\text{sphere,Pe}\to 0} = 2$, thus we introduce the normalized thermal power exchange $\hat{Q}$ as

$$\hat{Q} := \frac{Q}{Q_{\text{sphere,Pe}\to 0}} = \frac{\text{Nu}}{2}\,\frac{A}{A_{\text{sphere}}}\,. \tag{C.2}$$

In the following, we analyze the shape dependence of $\hat{Q}$ by systematically varying the aspect ratios λ_1, λ_2 and the shape exponents s_1, s_2, and plot the corresponding surfaces $\hat{Q} = \hat{Q}(\lambda_1, \lambda_2; \text{Pe})|_{s_1,s_2}$ and $\hat{Q} = \hat{Q}(s_1, s_2; \text{Pe})|_{\lambda_1,\lambda_2}$ at various Pe.

C.1. Varying the aspect ratios λ_1, λ_2

When considering the normalized thermal power exchange $\hat{Q} = \hat{Q}(\lambda_1, \lambda_2; \text{Pe})|_{s_1,s_2}$, the influence of aspect ratios changes compared to the trends observed for Nu (see Fig. C.4). Although Nu decreases with increasing aspect ratios, the increase in surface area A partially compensates for this reduction, so that $\hat{Q}$ exhibits a weaker sensitivity to aspect ratios than Nu. In all cases considered, $\hat{Q}$ shows a pronounced minimum in the near-spherical region and increases as λ_1, λ_2 grow, indicating that deviations from sphericity enhance the thermal power exchange of particles. Similarly to before, increasing Pe systematically increases $\hat{Q}$ due to convection enhancement, while for small Pe the $\hat{Q} = \hat{Q}(\lambda_1, \lambda_2; \text{Pe})|_{s_1,s_2}$ surfaces nearly collapse, with only minor differences between Pe = 0.01 and Pe = 0.001, consistent with a diffusion-dominated regime.

C.2. Varying the shape exponents s_1, s_2

Fig. C.5 shows the variation of the normalized thermal power exchange $\hat{Q} = \hat{Q}(s_1, s_2; \text{Pe})|_{\lambda_1,\lambda_2}$ as a function of the shape exponents s_1, s_2 for fixed aspect ratios λ_1, λ_2.

For given λ_1, λ_2, substantial variations in $\hat{Q}$ are observed for varying s_1, s_2. Depending on the shape exponents, the normalized thermal power exchange differs significantly, demonstrating the pronounced influence of s_1, s_2. This influence persists throughout all Pe considered, indicating that the observed trends are mainly shape-driven rather than flow-regime dependent.

In all cases, deviations from the ellipsoidal limit ($s_1 = s_2 = 1$) lead to notable changes in $\hat{Q}$. This highlights that differences in surface curvature distribution and local geometric features, which are not captured by aspect ratios alone, directly affect the combined influence of Nu and surface area A, showing that an ellipsoidal approximation does not provide sufficient accuracy across the complete superellipsoidal shape space considered here. Whether an ellipsoidal approximation is sufficiently accurate for a particular particle depends on the admissible modeling error, the Péclet number, and the procedure used to define an equivalent ellipsoid. A universal acceptability criterion is therefore not introduced here. The complete shape-resolved Nusselt-number data are

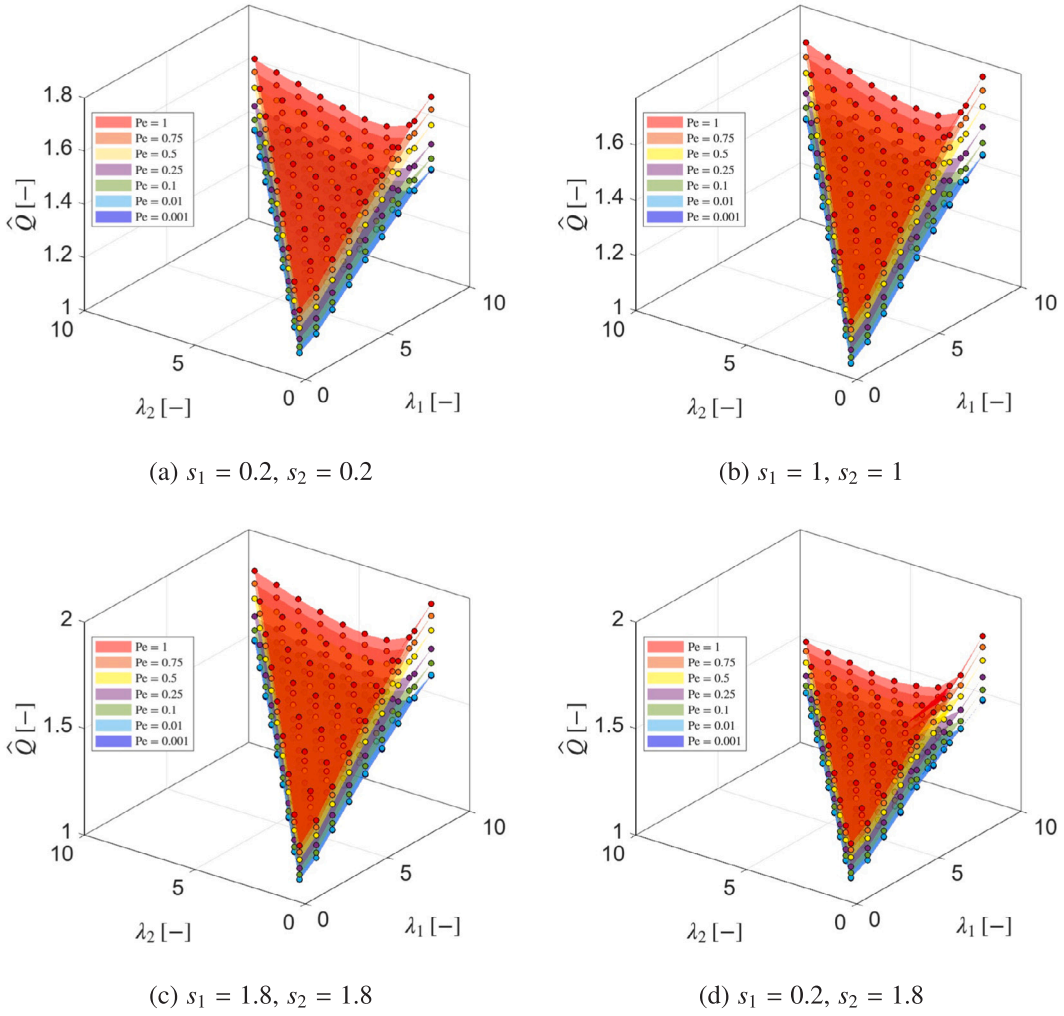


Fig. C.4. Normalized thermal power $\hat{Q}$ for superellipsoidal particles with fixed s_1, s_2 for varying aspect ratios λ_1, λ_2 at different Pe.

available in the accompanying Zenodo repository [30], enabling such application-specific comparisons.

We also observe that as the aspect ratios increase, the sensitivity of $\hat{Q}$ to variations in s_1, s_2 becomes more pronounced. Highly anisotropic particles exhibit steeper gradients in $\hat{Q}$ across the s_1, s_2 space, indicating a strong coupling between shape anisotropy and shape asymmetry. Consequently, for example, asymmetric particles with identical aspect ratios but different shape exponents can display notably different thermal power exchange.

In Fig. C.5(a) with $\lambda_1 = \lambda_2 = 1$, the minimum of $\hat{Q}$ is achieved for $s_1 = s_2 = 1$, that is, a sphere. From this limit, deviations toward more cubical ($s_1 = s_2 < 1$) or more diamond ($s_1 = s_2 > 1$) shapes lead to an increase in $\hat{Q}$. For anisotropic shapes ($\lambda_1, \lambda_2 > 1$), this behavior changes qualitatively. For prolate shapes ($\lambda_1 = 7, \lambda_2 = 1$), the minimum value of $\hat{Q}$ no longer occurs for the ellipsoidal case ($s_1 = s_2 = 1$), but instead changes to more cubical shapes. Also for oblate ($\lambda_1 = \lambda_2 > 1$) shapes, the location of the minimum $\hat{Q}$ changes and is likewise also no longer associated with the ellipsoidal case ($s_1 = s_2$). Instead, the lowest normalized thermal power exchanges are observed for asymmetric shapes with $s_1 \neq s_2$, reflecting the strong influence of asymmetric curvature distributions on the combined effect of Nu and A. This behavior highlights that the thermal power exchange depends sensitively on the detailed balance between shape anisotropy and asymmetry. Taken together, while the particle aspect ratios remain dominant shape parameters, the present results show that shape exponents introduce independent and significant contributions to the particle heat transfer coefficient, rendering ellipsoidal shape approximations insufficient for accurate heat transfer predictions.

Appendix D. Motivation for the choice of two Pe exponents

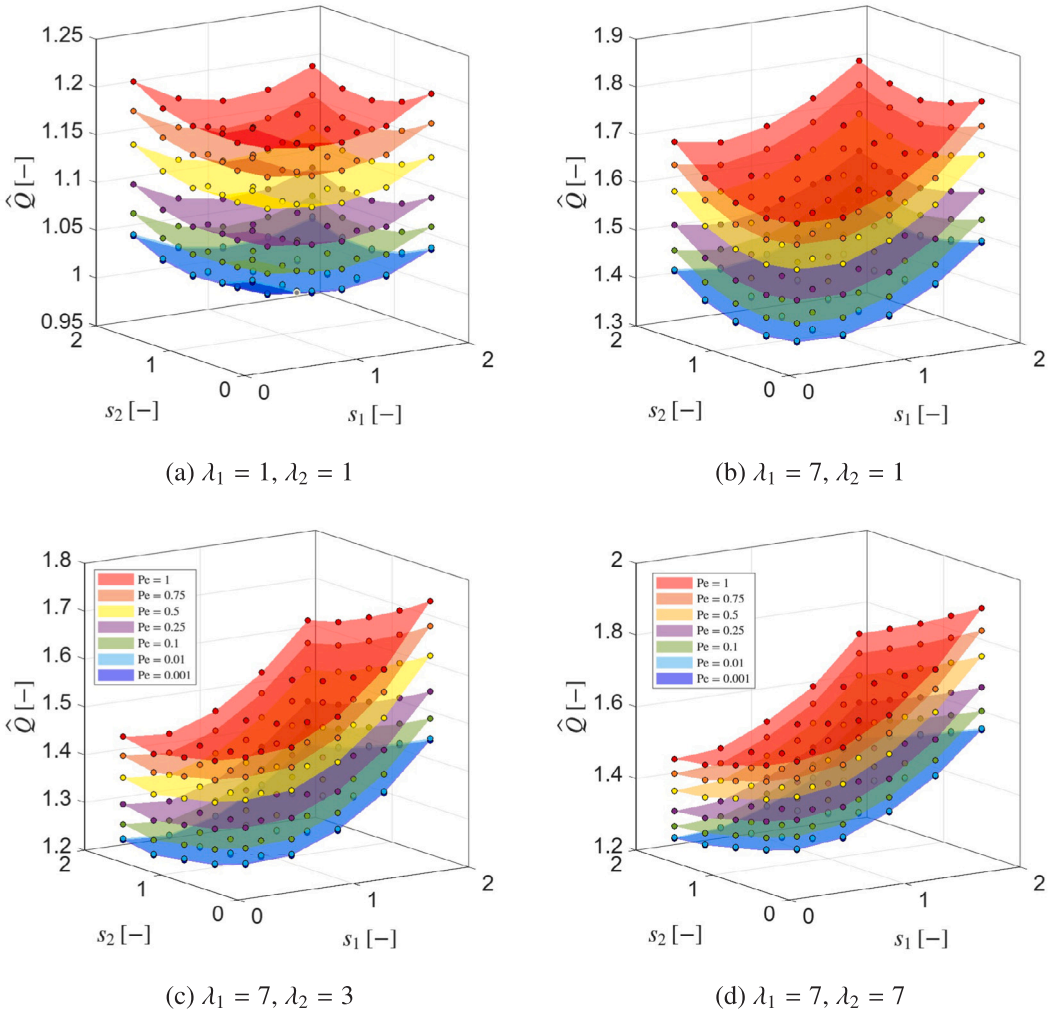
Note the use of two Pe exponents in Eq. (26), which is motivated by the observed scaling behavior of the convective enhancement. When the relative increment $g = \mathrm{Nu}/\mathrm{Nu}_0 - 1$ is plotted as a function of the normalized Péclet number $\mathrm{Pe}/\mathrm{Pe}_{\mathrm{ref}}$, the data do not collapse onto a single power-law curve with constant slope, see for example Fig. D.6 (a,b). Instead, the effective slope in log–log representation varies with Pe, with increasing deviation from the constant slope reference (see Fig. D.6 (a,b)), indicating a gradual transition between transport regimes.

To quantify the Péclet number scaling of the convective enhancement, we define a local effective exponent as the logarithmic derivative

$$m_{\mathrm{eff}}(\mathrm{Pe}) := \frac{\mathrm{d}\,\log g(\mathrm{Pe})}{\mathrm{d}\,\log \mathrm{Pe}}\,. \tag{D.1}$$

For a pure power-law dependence $g \sim \mathrm{Pe}^m$, the effective exponent reduces to the constant value m. Deviations from a constant m_{eff} therefore indicate non-single-exponent scaling. In practice, m_{eff} is estimated from the discrete data using finite differences in log–log space. As shown in Fig. D.7, m_{eff} varies strongly with Pe for all particle shapes displayed.

Consequently, we conclude that a single-term power-law correction of the form $\mathrm{Pe}^m \exp(\eta(\xi))$ is therefore insufficient to capture this behavior over the full range of Pe considered. Introducing two contributions



(a) $\lambda_1 = 1, \lambda_2 = 1$ (b) $\lambda_1 = 7, \lambda_2 = 1$

(c) $\lambda_1 = 7, \lambda_2 = 3$ (d) $\lambda_1 = 7, \lambda_2 = 7$

Fig. C.5. Normalized thermal power $\hat{Q}$ for superellipsoidal particles with fixed λ_1, λ_2 for varying shape exponents s_1, s_2 at different Pe.

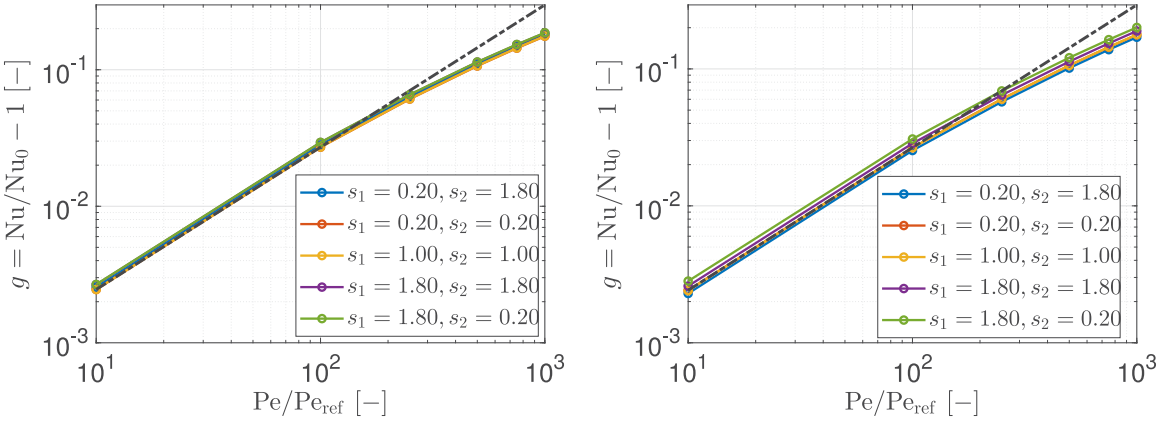


Fig. D.6. Scaling of the relative convective enhancement $g = \mathrm{Nu}/\mathrm{Nu}_0 - 1$ with the normalized Péclet number $\mathrm{Pe}/\mathrm{Pe}_{\mathrm{ref}}$ for fixed aspect ratios (a) $(\lambda_1, \lambda_2) = (5.0, 1.0)$ and (b) $(\lambda_1, \lambda_2) = (5.0, 5.0)$ and several shape exponent combinations (s_1, s_2). Note that $\mathrm{Pe}_{\mathrm{ref}} = 0.001$. Symbols denote simulation data, while the black dashed line indicates a reference power-law scaling obtained by fitting a straight line in log–log space between $\mathrm{Pe}/\mathrm{Pe}_{\mathrm{ref}} = 10$ and $\mathrm{Pe}/\mathrm{Pe}_{\mathrm{ref}} = 100$ for the reference shape exponents $s_1 = s_2 = 1.0$.

with distinct exponents allows the effective Péclet number scaling to vary smoothly, with the lower exponent dominating at moderate Pe and the higher exponent becoming relevant at larger Pe. This formulation represents the minimal extension required to reproduce the observed scaling trends while retaining a compact and interpretable structure.

Appendix E. Coefficients of the nusselt number correlation model

This appendix reports the retained terms and fitted coefficients obtained from the pruning procedure for the Nusselt number correlation model (see Tables E.11 and E.12).

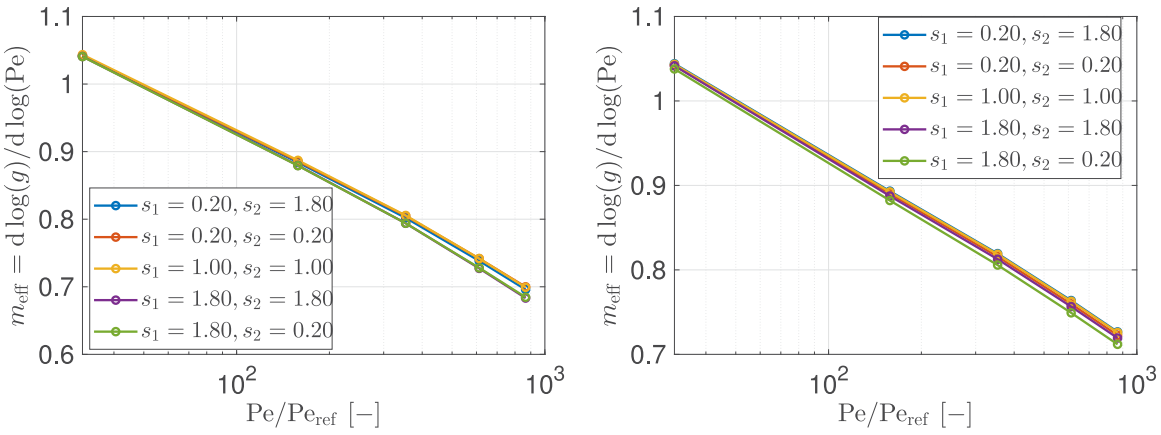


Fig. D.7. Local effective Péclet number exponent $m_{\mathrm{eff}} = \mathrm{d}\log(g)/\mathrm{d}\log(\mathrm{Pe})$ as a function of the normalized Péclet number $\mathrm{Pe}/\mathrm{Pe}_{\mathrm{ref}}$ for the same particle shapes shown in Fig. D.6. Note that $\mathrm{Pe}_{\mathrm{ref}} = 0.001$. The effective exponent is estimated from finite differences of the data in log–log space and represents the local slope of the curves in Fig. D.6.

Table E.11
Pruned terms and corresponding coefficients for ϕ^{η_a} with $a = 1, 2$.

Branch a	Local index i	$\phi_i^{\eta_a}$	Coefficient
1	0	1	$-1.9115509987 \times 10^{0}$
1	1	E_1	$2.9958302155 \times 10^{-2}$
1	2	E_1^2	$2.9966125730 \times 10^{-3}$
1	3	E_1^3	$1.1598255951 \times 10^{-3}$
1	4	E_2	$2.5403253734 \times 10^{-2}$
1	5	$E_1^3 S_1$	$1.3249645708 \times 10^{-3}$
2	0	1	$-6.9491953850 \times 10^{0}$
2	1	E_1	$-1.2821632624 \times 10^{0}$
2	2	E_1^2	$1.5268760920 \times 10^{0}$
2	3	E_1^3	$-4.4652757049 \times 10^{-1}$
2	4	E_2	$7.1352154016 \times 10^{-1}$
2	5	E_2^3	$-4.0747854859 \times 10^{-2}$
2	6	$E_1^2 E_2$	$-1.0859798640 \times 10^{-1}$
2	7	$E_1^3 S_1$	$2.8103733435 \times 10^{-2}$
2	8	$E_1^3 S_2$	$-2.4252904952 \times 10^{-1}$
2	9	$E_2^3 S_1$	$4.9520283937 \times 10^{-2}$

Table E.12
Pruned terms and corresponding coefficients for $\Phi_{0,a}$.

Local index i	Φ_i^0	Coefficient
0	1	$1.9218347073 \times 10^{0}$
1	E_1	$-5.3360417485 \times 10^{-2}$
2	E_1^2	$-6.8294994533 \times 10^{-2}$
3	E_1^3	$6.2844292261 \times 10^{-3}$
4	E_2	$-6.6822066903 \times 10^{-2}$
5	E_2^2	$-3.0540449079 \times 10^{-3}$
6	E_2^3	$-2.3947229784 \times 10^{-4}$
7	$E_1 E_2$	$4.6479325742 \times 10^{-2}$
8	$E_1^2 E_2$	$-5.9868698008 \times 10^{-3}$
9	$E_1 E_2^2$	$2.4593584239 \times 10^{-3}$
10	S_1^2	$-2.0558834076 \times 10^{-1}$
11	S_2^2	$-1.1550086737 \times 10^{-1}$
12	$E_1 S_1$	$-5.8672282845 \times 10^{-2}$
13	$E_2 S_1$	$9.3803098425 \times 10^{-3}$
14	$E_2 S_1 S_2$	$1.2804592960 \times 10^{-2}$
15	$E_1^2 S_1$	$-2.2325141355 \times 10^{-2}$
16	$E_1^2 S_2$	$2.6369996369 \times 10^{-2}$
17	$E_1^3 S_1$	$4.0929019451 \times 10^{-3}$
18	$E_1^3 S_2$	$-4.8993737437 \times 10^{-3}$
19	$E_2^2 S_1$	$5.2487556823 \times 10^{-3}$
20	$E_2^2 S_2$	$-2.1137227304 \times 10^{-3}$
21	$E_2^3 S_1$	$-4.3002743041 \times 10^{-4}$
22	$E_2^3 S_2$	$1.4333735453 \times 10^{-4}$
23	$E_1 S_2^2$	$4.2779780924 \times 10^{-2}$
24	$E_1 S_1^3$	$1.1613506824 \times 10^{-2}$

Table F.13
Influence of the PCNN architecture on the test-set performance. The quantity $\mathrm{NMSE}_{\mathrm{best}}$ denotes the lowest test NMSE among the repeated training runs. The relative error for test sample i is defined as $\epsilon^i_{\mathrm{rel}} = \left|\left[\mathrm{Nu}^i_{\mathrm{PCNN}} - \mathrm{Nu}^i_{\mathrm{DNS}}\right]/\mathrm{Nu}^i_{\mathrm{DNS}}\right|$ [%]. The column $\max(\epsilon_{\mathrm{rel}})$ reports the mean and standard deviation of the maximum test-set relative error over the repeated runs. All quantities except $\mathrm{NMSE}_{\mathrm{best}}$ are reported as mean ± standard deviation over ten training runs.

Architecture	Parameters	$\mathrm{NMSE}_{\mathrm{best}}$	$\mathrm{NMSE}_{\mathrm{mean}}$	R^2_{test}	$\max(\epsilon_{\mathrm{rel}})$ [%]
(2, 2)	40	2.86×10^{-4}	$[3.79 \pm 3.33] \times 10^{-3}$	0.832077 ± 0.144856	22.49 ± 14.48
(4, 4)	94	2.55×10^{-5}	$[9.04 \pm 8.18] \times 10^{-5}$	0.995528 ± 0.003935	4.50 ± 1.87
(4, 4, 2)	110	2.34×10^{-5}	$[6.01 \pm 4.44] \times 10^{-5}$	0.997047 ± 0.002199	3.96 ± 1.43
(6, 6)	164	4.34×10^{-6}	$[1.60 \pm 0.66] \times 10^{-5}$	0.999299 ± 0.000307	1.87 ± 0.48
(6, 6, 4)	216	5.96×10^{-6}	$[1.00 \pm 0.39] \times 10^{-5}$	0.999533 ± 0.000147	1.46 ± 0.34

Appendix F. PCNN architecture comparison

To assess whether the number of neurons could be reduced without a substantial loss of predictive accuracy, several smaller PCNN architectures were trained using identical data partitions, optimization settings, stopping criteria, and ten independent initializations. The comparison is summarized in Table F.13. The smallest architecture, $(2, 2)$, exhibits a pronounced reduction in accuracy and a large variability between repeated training runs. Increasing the network size to $(4, 4)$ or $(4, 4, 2)$ substantially improves the predictions, but both architectures still show larger mean test errors and larger run-to-run variations than the two widest configurations.

The $(6, 6)$ architecture yields the lowest value of $\mathrm{NMSE}_{\mathrm{best}}$, indicating that an individual training run can achieve very high accuracy with this reduced model. However, architecture selection should not be based solely on the best realization. Over ten repeated runs, the selected $(6, 6, 4)$ architecture provides the lowest mean evaluation-subset NMSE, $[1.00 \pm 0.39] \times 10^{-5}$, compared with $[1.60 \pm 0.66] \times 10^{-5}$ for $(6, 6)$. It also achieves the largest mean test coefficient of determination, $R^2_{\mathrm{test}} = 0.999533 \pm 0.000147$, and the lowest mean maximum relative error, $1.46 \pm 0.34\%$. In addition, the smaller standard deviations indicate a more reproducible performance across different initializations.

The complete $(6, 6, 4)$ PCNN contains only 216 trainable parameters. Thus, the additional 52 parameters relative to the $(6, 6)$ network produce a measurable improvement in average accuracy and robustness while adding only a negligible storage and evaluation cost. The $(6, 6, 4)$ architecture was therefore chosen as the best compromise between compactness, predictive accuracy, and robustness.

References

[1] W.E. Ranz, W.R. Marshall, Evaporation from drops, Chem. Eng. Prog. 48 (1952) 141–146.

[2] S. Whitaker, Forced convection heat transfer correlations for flow in pipes, past flat plates, single cylinders, single spheres, and for flow in packed beds and tube bundles, AIChE J. 18 (2) (1972) 361–371, http://dx.doi.org/10.1002/aic.690180219.

[3] T. Kiwitt, K. Fröhlich, M. Meinke, W. Schröder, Nusselt correlation for ellipsoidal particles, Int. J. Multiph. Flow 149 (2022) 103941, http://dx.doi.org/10.1016/j.ijmultiphaseflow.2021.103941.

[4] N. Ellendt, A. Lumanglas, S.I. Moqadam, L. Mädler, A model for the drag and heat transfer of spheres in the laminar regime at high temperature differences, Int. J. Therm. Sci. 133 (2018) 98–105.

[5] J. Wiskel, H. Henein, E. Maire, Solidification study of aluminum alloys using impulse atomization: Part I - Heat transfer analysis of an atomized droplet, Can. Metall. Q. 41 (1) (2002) 97–110, http://dx.doi.org/10.1179/cmq.2002.41.1.97.

[6] H. Brenner, Forced convection heat and mass transfer at small péclet numbers from a particle of arbitrary shape, Chem. Eng. Sci. 18 (2) (1963) 109–122, http://dx.doi.org/10.1016/0009-2509(63)80020-2.

[7] A. Acrivos, A note on the rate of heat or mass transfer from a small particle freely suspended in a linear shear field, J. Fluid Mech. 98 (2) (1980) 299–304, http://dx.doi.org/10.1017/S002211208000016X.

[8] H.A. Dwyer, D.S. Dandy, Some influences of particle shape on drag and heat transfer, Phys. Fluids A 2 (12) (1990) 2110–2118.

[9] S.W. Churchill, M. Bernstein, A correlating equation for forced convection from gases and liquids to a circular cylinder in crossflow, J. Heat Transf. 99 (2) (1977) 300–306, http://dx.doi.org/10.1115/1.3450685.

[10] F.P. Incropera, D.P. DeWitt, T.L. Bergman, A.S. Lavine, Fundamentals of Heat and Mass Transfer, Sixth ed., John Wiley & Sons, Hoboken, NJ, 2007.

[11] C. Ke, S. Shu, H. Zhang, H. Yuan, Drag coefficient and averaged nusselt number of a scalene prolate ellipsoid, Appl. Math. Model. 64 (2018) 556–571, http://dx.doi.org/10.1016/j.apm.2018.07.055, URL https://www.sciencedirect.com/science/article/pii/S0307904X18303731.

[12] C.A. Zuritz, S.C. McCoy, S.K. Sastry, Convective heat transfer coefficients for irregular particles immersed in non-newtonian fluid during tube flow, J. Food Eng. 11 (2) (1990) 159–174, http://dx.doi.org/10.1016/0260-8774(90)90051-9.

[13] A. Richter, P.A. Nikrityuk, New correlations for heat and fluid flow past ellipsoidal and cubic particles at different angles of attack, Powder Technol. 249 (2013) 463–474, http://dx.doi.org/10.1016/j.powtec.2013.08.044, URL https://www.sciencedirect.com/science/article/pii/S0032591013005743.

[14] N. Kishore, S. Gu, Momentum and heat transfer phenomena of spheroid particles at moderate Reynolds and Prandtl numbers, Int. J. Heat Mass Transfer 54 (11) (2011) 2595–2601.

[15] C. Ke, S. Shu, H. Zhang, H. Yuan, D. Yang, On the drag coefficient and averaged nusselt number of an ellipsoidal particle in a fluid, Powder Technol. 325 (2018) 134–144, http://dx.doi.org/10.1016/j.powtec.2017.10.049.

[16] H. Ma, Y. Zhao, Convective heat transfer coefficient for a rod-like particle in a uniform flow, Int. J. Heat Mass Transfer 147 (2020) 118742, http://dx.doi.org/10.1016/j.ijheatmasstransfer.2019.118742.

[17] D.A. Lote, X. Yang, M. Khalij, B. Arcen, A. Tanière, X. Mao, The nusselt number and the aerodynamic coefficients for prolate and cylindrical particles at low to moderate Reynolds number, Powder Technol. 464 (2025) 121131, http://dx.doi.org/10.1016/j.powtec.2025.121131.

[18] L. Xu, D.A. Lote, X. Yang, M. Khalij, B. Arcen, A. Tanière, C. Zhang, X. Mao, The nusselt number and the aerodynamic coefficients for oblate particles from Stokes limit to high Reynolds number, Int. J. Multiph. Flow 200 (2026) 105710, http://dx.doi.org/10.1016/j.ijmultiphaseflow.2026.105710.

[19] A.H. Barr, Superquadrics and Angle-Preserving Transformations, IEEE Comput. Graph. Appl. 1 (1) (1981) 11–23.

[20] J. Wedel, P. Steinmann, M. Štrakl, M. Hriberšek, J. Ravnik, Shape matters: Lagrangian tracking of complex nonspherical microparticles in superellipsoidal approximation, Int. J. Multiph. Flow 158 (2023) 104283, http://dx.doi.org/10.1016/j.ijmultiphaseflow.2022.104283.

[21] J. Wedel, M. Hriberšek, J. Ravnik, P. Steinmann, A novel pseudo-rigid body approach to the non-linear dynamics of soft micro-particles in dilute viscous flow, J. Comput. Phys. 519 (2024) 113377, http://dx.doi.org/10.1016/j.jcp.2024.113377.

[22] OpenFOAM The OpenFOAM Foundation, OpenFOAM Foundation repository for OpenFOAM version 11, 2024, URL https://github.com/OpenFOAM/OpenFOAM-11, (Accessed 18 November 2024).

[23] K. Kiger, C. Pan, E. Lindborg, A. Johansson, J. Eaton, J. Humphrey, N. Kasagi, M. Leschziner, M. Sommerfeld, Suspension and turbulence modification effects of solid particulates on a horizontal turbulent channel flow, JoT 3 (2002) 27–29.

[24] K.O. Fong, O. Amili, F. Coletti, Velocity and spatial distribution of inertial particles in a turbulent channel flow, J. Fluid Mech. 872 (2019) 367–406, http://dx.doi.org/10.1017/jfm.2019.355.

[25] M. Esmaily, L. Villafane, A. Banko, G. Iaccarino, J. Eaton, A. Mani, A benchmark for particle-laden turbulent duct flow: A joint computational and experimental study, Int. J. Multiph. Flow 132 (2020) 103410, http://dx.doi.org/10.1016/j.ijmultiphaseflow.2020.103410.

[26] P. Costa, L. Brandt, F. Picano, Interface-resolved simulations of small inertial particles in turbulent channel flow, J. Fluid Mech. 883 (2020) A54, http://dx.doi.org/10.1017/jfm.2019.918.

[27] M. Štrakl, M. Hriberšek, J. Wedel, P. Steinmann, J. Ravnik, A Model for Translation and Rotation Resistance Tensors for Superellipsoidal Particles in Stokes Flow, J. Mar. Sci. Eng. 10 (3) (2022) 369.

[28] A. Jaklič, A. Leonardis, F. Solina, Superquadrics and their geometric properties, 20, 2000, pp. 13–39.

[29] A. Jaklič, F. Solina, Moments of superellipsoids and their application to range image registration, IEEE Trans. Syst. Man, Cybern. Part B, Cybern.: A Publ. the IEEE Syst. Man, Cybernetics Soc. 33 (2003) 648–657.

[30] J. Wedel, I.D. Horvat, M. Hriberšek, P. Steinmann, J. Ravnik, Physics-constrained neural network model for Nusselt number prediction for superellipsoidal particles in flows, 2026, http://dx.doi.org/10.5281/zenodo.21259577, URL https://doi.org/10.5281/zenodo.21259577.

[31] A. Acrivos, T.D. Taylor, Heat and mass transfer from single spheres in Stokes flow, Phys. Fluids 5 (4) (1962) 387–394, http://dx.doi.org/10.1063/1.1706630.

[32] D.P. Kingma, J. Ba, Adam: A method for stochastic optimization, 2014, CoRR, arXiv:1412.6980.

[33] I. Loshchilov, F. Hutter, Decoupled weight decay regularization, in: International Conference on Learning Representations, 2017.

[34] Z. Hao, S. Liu, Y. Zhang, C. Ying, Y. Feng, H. Su, J. Zhu, Physics-informed machine learning: A survey on problems, methods and applications, 2023, arXiv:2211.08064.

[35] Y. Zhu, N. Zabaras, P.-S. Koutsourelakis, P. Perdikaris, Physics-constrained deep learning for high-dimensional surrogate modeling and uncertainty quantification without labeled data, J. Comput. Phys. 394 (2019) 56–81.

[36] T. Beucler, M. Pritchard, S. Rasp, J. Ott, P. Baldi, P. Gentine, Enforcing analytic constraints in neural networks emulating physical systems, Phys. Rev. Lett. 126 (9) (2021) http://dx.doi.org/10.1103/physrevlett.126.098302.

[37] J. Happel, H. Brenner, Low Reynolds Number Hydrodynamics, Martinus Nijhoff Publishers, Kluwer, The Hague, Netherlands, 1983.